

Manuscript Number:

Title: Detection and evaluation of damage in aircraft composites using  
electromagnetically coupled spiral inductors

Article Type: Full Length Article

Keywords: carbon-fibre reinforced polymer (CFRP); non-destructive testing  
(NDT); electromagnetic sensor; coupled spiral inductors; equivalent  
circuit modelling; damage evaluation

Corresponding Author: Prof. Constantinos Soutis, PhD

Corresponding Author's Institution: University of Manchester

First Author: Zhen Li

Order of Authors: Zhen Li; Arthur Haigh; Constantinos Soutis, PhD;  
Andrew Gibson; Robin Sloan; Noushin Karimian

Abstract: The paper presents a quantitative damage evaluation of carbon-fibre reinforced polymer (CFRP) plates using a non-contact electromagnetic (EM) sensor. The EM sensor with coupled spiral inductors (CSI) is employed here to detect both impact induced and simulated damage leading to an accurate evaluation of the location, depth and width of sub-surface defects. The effect of inspection frequency, standoff distance and signal power are also investigated leading to the development of an engineering circuit design tool that relates the set up and calibration of the sensor to its detection performance. It is found that the dynamic range of the transmission coefficient is the limiting factor in the original Salski CSI sensor and this problem is addressed by adding ferrite layers to reduce the reluctance of the magnetic circuit, improving damage sensing by 22%. The study leads to a further development of utilising an open ferrite yoke with a pair of encircling coils, which shows a 57 % sensitivity improvement and clearer identification of air gaps (voids) and delamination in CFRP laminates. The proposed EM yoke CSI sensor is of low cost and could be assembled into an array for non-contact, in situ mechatronic scanning of aircraft composite wings.

Suggested Reviewers: Victor Giurgiutiu PhD  
Professor, Engineering, University of South Carolina  
VICTORG@sc.edu  
expert on NDT sensors and composite structures

Robert Smith PhD  
Professor, University of Bristol  
Robert.Smith@bristol.ac.uk  
NDT expert and composites

**Covering letter for submission of a paper to *Composite Structures***

Constantinos Soutis

Aerospace Research Institute,

The University of Manchester

Manchester, M13 9PL, UK

Dear Professor Ferreira,

We wish to submit a new manuscript entitled “*Detection and evaluation of damage in aircraft composites using electromagnetically coupled spiral inductors*” for your consideration.

We do confirm that this work is original and has not been published elsewhere nor is it currently under consideration for publication elsewhere.

In this paper, we report a quantitative damage evaluation of carbon-fibre reinforced polymer (CFRP) plates using a non-contact electromagnetic (EM) sensor. The EM sensor with coupled spiral inductors (CSI) is employed here to detect both impact induced and simulated damage leading to an accurate evaluation of the location, depth and width of sub-surface defects. The effect of inspection frequency, standoff distance and signal power are also investigated leading to the development of an engineering circuit design tool that relates the set up and calibration of the sensor to its detection performance. It is found that the dynamic range of the transmission coefficient is the limiting factor in the original CSI sensor and this problem is addressed by adding ferrite layers to reduce the reluctance of the magnetic circuit, improving damage sensing by 22%. The study leads to a further development of utilising an open ferrite yoke with a pair of encircling coils, which shows a 57 % sensitivity improvement and clearer identification of air gaps (voids) and delamination in CFRP laminates. The proposed EM yoke CSI sensor is of low cost and could be assembled into an array for non-contact, in situ mechatronic scanning of aircraft composite wings.

The paper will be of interest to readers in the area of nondestructive evaluation of composite structures.

Please address all correspondence concerning this manuscript to

[constantinos.soutis@manchester.ac.uk](mailto:constantinos.soutis@manchester.ac.uk).

Thank you for your consideration of this manuscript.

Your sincerely,

Constantinos Soutis

Detection and evaluation of damage in aircraft composites  
using electromagnetically coupled spiral inductors

Zhen Li<sup>a</sup>, Arthur Haigh<sup>b</sup>, Constantinos Soutis<sup>a, c\*</sup>, Andrew Gibson<sup>c</sup>,  
Robin Sloan<sup>b</sup> and Noushin Karimian<sup>c</sup>

<sup>a</sup>Aerospace Research Institute, <sup>b</sup>School of Electrical and Electronic Engineering,

<sup>c</sup>School of Mechanical, Aerospace and Civil Engineering

The University of Manchester, Manchester, M13 9PL, UK

\*Corresponding author: constantinos.soutis@manchester.ac.uk

**Abstract**

The paper presents a quantitative damage evaluation of carbon-fibre reinforced polymer (CFRP) plates using a non-contact electromagnetic (EM) sensor. The EM sensor with coupled spiral inductors (CSI) is employed here to detect both impact induced and simulated damage leading to an accurate evaluation of the location, depth and width of sub-surface defects. The effect of inspection frequency, standoff distance and signal power are also investigated leading to the development of an engineering circuit design tool that relates the set up and calibration of the sensor to its detection performance. It is found that the dynamic range of the transmission coefficient is the limiting factor in the original Salski CSI sensor and this problem is addressed by adding ferrite layers to reduce the reluctance of the magnetic circuit, improving damage sensing by 22%. The study leads to a further development of utilising an open ferrite yoke with a pair of encircling coils, which shows a 57 % sensitivity improvement and clearer identification of air gaps (voids) and delamination in CFRP laminates. The proposed EM yoke CSI sensor is of low cost and could be assembled into an array for non-contact, in situ mechatronic scanning of aircraft composite wings.

**Keywords:** carbon-fibre reinforced polymer (CFRP); non-destructive testing (NDT);  
electromagnetic sensor; coupled spiral inductors; equivalent circuit modelling; damage evaluation;

## 1. Introduction

The proportion of fibre composite materials being used in aerospace, industrial, automotive and marine structures is increasing year on year. Continuously reinforced thermosets are currently the most popular composite systems, since they are offering better fatigue and corrosion resistance, higher specific stiffness and strength when compared to conventional metallic materials. They can be found in new aircraft such as the Boeing 787 Dreamliner and Airbus A350 XWB (extra wide body), which are now at various stages in the design/manufacture/certification/delivery cycle. One of the most difficult problems to be overcome during the certification process of such aircraft by the civil aviation authorities for safe commercial use is to guarantee their structural integrity over the 30 years life of the aircraft [1]. This is technologically challenging for large integral composite structures, with wing spans of more than 25 m, fuselage barrel lengths of 50 m and diameter 5 m .

Although carbon fibre-epoxy composites are used more extensively in civil aircraft structures [1], they remain vulnerable to impact damage (e.g., bird strike, hail, tyre rubber and metal fragments), due to their relatively thin composite skins and brittle behaviour. Continuous degradation can, in turn, affect structural performance over time, such that structural integrity is a major problem for the industry as it seeks a viable strategy for design and certification of large composite aircraft structures subjected to impact damage. Some types of fabrication defects and in-service damage cannot be identified or evaluated by a visual observation. Hence, various non-destructive testing (NDT) techniques have been employed to identify defects and damage in CFRP composites [2], for example, ultrasonic testing [3], eddy current technique (ECT) [4], thermography, X-ray tomography, optical fibre sensors, digital image correlation (DIC) [6], Lamb waves [6] and microwave techniques [7,8]. While, every NDT method has its own particular advantages, disadvantages and applications, some aspects (i.e., types of damage to be monitored, detection reliability, cost, portability, equipment

1 setup, scanning time, safety concerns and measurement sensitivity) have to be selected and well  
2  
3 understood by the user.  
4

5 Among the existing NDT techniques, a group of electromagnetic (EM) techniques are receiving  
6  
7 increasing attention in recent years, including eddy current, pulsed eddy current and microwave  
8  
9 techniques. There are a number of attributes when applying the EM NDT, such as non-contact, one-  
10  
11 sided scanning, no need for transducers or couplants, little safety hazard [9]. For this kind of  
12  
13 electromagnetic non-destructive testing, special attention should be paid to the penetration depth of  
14  
15 the signal into the sample, which is inversely proportional to the square root of the operating  
16  
17 frequency and the conductivity of the sample [9].  
18  
19  
20  
21

22 Recently, Salski et al. [10–12] proposed a new type of electromagnetic sensor for CFRP composites.  
23  
24 The designed sensor with coupled spiral inductors (CSI) exhibits several advantages, such as low  
25  
26 power (~10 mW), low cost (less than £10), operator friendly and conformability (flexible printed  
27  
28 circuit board). It operates at the radio frequencies where the penetration depth is comparable with the  
29  
30 thickness of the composite [10]. The capability of detecting an air gap and cracks intentionally  
31  
32 produced in a four-layer CFRP composite plate was reported.  
33  
34  
35  
36

37 In the present paper, the Salski CSI sensor [10] has been reproduced with design improvements on  
38  
39 impedance matching and configuration. It is used to detect six subsurface grooves that simulate  
40  
41 manufacturing defects and delaminations (seen as air gaps, voids) in CFRP composites. A thorough  
42  
43 discussion on the quantitative description of damage, location, size and interaction is presented.  
44  
45 Subsequently, some parametric studies investigating the effects of inspection frequency, standoff  
46  
47 distance and signal power are conducted. Based on the parametric study, the proposed equivalent  
48  
49 circuit model provides an engineering design tool that relates the CSI geometry (e.g. number of  
50  
51 inductor turns) and setup (e.g. frequency and standoff distance) to detection performance. Further,  
52  
53 the application is extended to the detection of barely visible impact damage (BVID) on a CFRP  
54  
55  
56  
57  
58  
59  
60  
61  
62  
63  
64  
65

composite plate. The magnetic reluctance of the CSI sensor is reduced by adding ferrite layers that improve its sensing by 22%. Finally, a refined design with a ferrite yoke and a pair of encircling coils improves the detection by 57%. The effective detection of a delamination layer is then demonstrated.

## **2. The CSI sensor**

### *2.1. Mechanism of the sensor*

Two coupled planar spiral inductors are fabricated on the underside of a printed circuit board (PCB). Using via holes, each inductor is connected to a coplanar transmission line on the top side to make a two port sensing device, as presented in Fig.1.

The principle of the detection is based on the measurement of the scattering transmission coefficient ( $S_{21}$ ), which defines the relative power transmitted from the primary spiral to the secondary spiral.  $S_{21}$  is selected rather than other S-parameters because a higher signal-to-noise ratio (SNR) can be provided. When a conductive material is placed in the vicinity of the CSI sensor, the reference  $S_{21}$  is obtained. A defect (dent, crack and delamination) in the material under test disturbs the coupling and perturbs  $S_{21}$  to enable detection and evaluation.

### *2.2. Experimental setup*

In the present work, Salski's design is optimised to ensure impedance matching and the final dimensions of the sensor are 38.4 mm long by 7.8 mm wide [13]. The sensor is mounted on an XYZ scanning stage and connected to HP8753B vector network analyser (VNA) by two coaxial cables. As schematically illustrated in Fig.2, the personal computer (PC) is connected to the controller of the stepper motors. The logic control for the stepper motors is managed by the PIC18C452 Microchip® microcontroller. All the movements are controlled by the PC using VEE software® for precise and reproducible movements. In addition, the analyser is connected to the PC by the IEEE-488 connection for data acquisition.

### 3. Damage detection and evaluation using the CSI sensor

#### 3.1. Non-contact detection of the intentionally produced grooves

Subsurface grooves are intentionally produced on a CFRP strip. The cross section of the composite strip is illustrated in Fig.3, where six grooves were machined on the bottom side. The ability of detecting the presence of the underneath defects is examined. The thickness of the strip is 2.58 mm, while the depths of the grooves from the left to right are 1.18 mm, 1.66 mm, 0.80 mm, 1.28 mm, 1.76 mm and 1.12 mm, respectively; the six grooves are 21.00 mm apart.

A non-contact line scanning is conducted across the CFRP strip with the step size of  $126.7 \mu\text{m}$ . The standoff distance between the sensor and the surface is kept constant at  $250 \mu\text{m}$ . Total scanning distance is 139.20 mm. During the scanning, the output power of the signal is set to be 0 dBm (i.e. 1 mW). The performance of the sensor at 10 MHz is examined. The optimal frequency for inspection will be investigated in section 3.4.1. By comparing the difference of the magnitude of the transmission coefficient (i.e.  $|S_{21}|$ ) between the origin and the present position, the sensitivity  $\Delta|S_{21}|$  at the selected frequency with respect to the scanning distance is shown in the left top of Fig.4. Six peaks of variable magnitudes indicating six grooves are accurately identified.

It is also shown that the variation of  $|S_{21}|$  only happens when the coupling region (i.e. the space under the inductor) interacts with the groove, i.e. between two critical positions where the coupling region starts to move across and leaves the boundaries of the groove. For example, for the first groove, the size of the affected region is the sum of the narrow dimension of the coupling region (6mm) and the width of the groove (4mm). The interaction can be further decomposed, considering the relative distance between the centre and the groove. As shown in the right part of Fig.4, the variations of the sensitivity between four critical positions (Position A, B, C and D) are analysed. Position A is in the

centre of the sensor, where the coupling region starts to scan across the left boundary of the groove. In the measurement process, the data is stored at the central point of the coupling region. In the sensitivity graph, the curve continues to rise until the coupling centre arrives at the left boundary of the groove (Position B), as the influence of the defect on the coupling becomes gradually prominent over this period. Afterwards, during the time when the coupling centre is still above the groove, the sensitivity value stabilises until the centre reaches Position C, where the centre comes to the right boundary of the groove. For symmetry reasons, the sensitivity drops as the centre moves away from the groove. At position D, the sensitivity declines to zero. In summary, when the sensor scans across each groove, the sensitivity curve experiences three stages, i.e. increasing (denoted as Stage I) between Position A and Position B, temporarily stable (denoted as Stage II) between Position B and Position C, and decreasing (denoted as Stage III) between Position C and Position D. If the width of the coupling region is denoted as  $L$  and that of the groove is described as  $W$ , then the widths of three stages are  $L/2$ ,  $W$  and  $L/2$ , respectively. In addition, the middle part of Stage II coincides with that of the groove. It is seen that Stage II is more distinct than other two stages. Therefore, this platform characteristic of Stage II is considerably beneficial for the evaluation of the width of the subsurface defect.

### *3.2. Relationship between the magnitude of the signal and the subsurface depth*

The highest peak exists at the location of the third groove counted from left to right, where the groove is the shallowest. While, the peak corresponding to the fifth groove is the lowest as expected. As listed in Table 1, there is a close relationship between the subsurface depth ( $h$ ) and the average magnitude of the signal in Stage II ( $H$ ). And in Fig.5 a linear line is offered by using regression analysis. The correlation coefficient  $R^2=0.97$  is given, which shows the high reliability of the approximation.



### 3.3. Discussion on the spatial resolution

Spatial resolution of an imaging system is regarded as its capability to separate two closely spaced defects. In the present case, if two grooves are closely located, Stage I of one defect and Stage III of the adjacent defect would overlap. Attention should be paid to the fact that the amplitude of Stage II is dependent on the subsurface depth of the defect. Hence, the defects located at the same depth could not be separated from the sensitivity curve if the distance between the adjacent grooves is larger than the width of Stage III, which is  $L/2$  (3.00 mm). However, two defects located at different depths can still be distinguished even though the separation is smaller than  $L/2$ , as long as the variation of the subsurface depth are detectable by the analyser.

### 3.4. Parametric study

#### 3.4.1. Effect of the inspection frequency

Following Salski [10], the sensitivity of  $S_{21}$  in the range 0-100 MHz is examined. Fig.6 (a) illustrates the frequency response of Groove 1 where the optimum response is observed around 10 MHz. The six-groove CFRP strip was then scanned at 5,10 ,15 and 20 MHz, respectively. In Fig. 6 (b), 10 MHz consistently produces the optimum sensor response.

#### 3.4.2. Effect of the standoff distance

A parametric study in the absence of machined grooves is performed to analyse the characteristic of  $|S_{21}|$  as a function of the standoff distance. The results of the parametric study are shown in Fig.7, where the standoff distance is increased from 0 to 5000  $\mu\text{m}$  for three frequencies (10 MHz, 20 MHz and 50 MHz). Typically the signal increases with the standoff distance and this asymptotes to the free space condition.

### 3.4.3. Effect of the signal power

In this section, the influence of different power levels is also investigated with the fixed standoff distance of 100  $\mu\text{m}$ . It is found that the increase of the signal power induces small variations of  $|S_{21}|$  (within 0.06 dB). It is suggested that the signal chosen at a lower power level is a beneficial factor for the practical application.

### 3.5. Detection of impact damage

In this section, the sensor is applied to detect the real impact damage on a 4 mm thick carbon fibre-epoxy +45/-45/0/90 quasi-isotropic plate. The barely visible impact damage (BVID) on the top surface was created by a drop-weight impact of 20 J energy. The diameter and depth of the dent observed by an optical laboratory microscope are approximately 3.85 mm and 44.3  $\mu\text{m}$ , respectively. This dent could not be easily found during general visual inspection using typical lighting conditions. A 2D raster scanning is performed with a step size of 381  $\mu\text{m}$  in both in-plane directions. A 2D image of the magnitude of  $S_{21}$  at the frequency 300 MHz is shown in Fig. 8. The median filtering and mean filtering are applied in the image post-processing for noise reduction and edge enhancement. The white area showing higher magnitudes evidently indicates the presence, location and extent of the dent. Further work will be required to identify other resin microcracks and delamination depth or separate multiple delaminations occurring during the impact event.

## 4. Equivalent circuit modelling

The purpose of this section is to derive an engineering design tool that can be used to estimate the  $S_{21}$  sensitivity of the sensor as a function of its geometry (e.g. number to turns of the coil), frequency and standoff distance. The geometry of the defect and electrical conductivity of the sample are also important. An equivalent lumped circuit model shown in Fig.9 can be derived for the measured setup.

According to the Kirchhoff's law [14], the transmission coefficient  $|S_{21}|$  is defined as:

$$|S_{21}| = \frac{MR_0}{\sqrt{\left[\frac{R_1(R_0 + R_2)}{\omega} + (M^2 - L_1L_2)\omega\right]^2 + (R_1L_1 + R_0L_1 + R_2L_1)^2}} \quad (1)$$

Where  $\omega = 2\pi f$  is the angular frequency while  $f$  is the operating frequency;  $R_1$  and  $L_1$  are the resistance and inductance of the feed coil, respectively;  $R_2$  and  $L_2$  are the resistance and inductance of the detector coil, respectively;  $R_0$  is the matched load ( $50 \Omega$ ) at Port 2;  $M$  is the mutual inductance between two inductors. Without losing generality, the value of  $M$  is set to be  $M = kL_1$ . The coupling coefficient  $k$  is linked to the standoff distance and conductivity distribution within the penetration depth. It is assumed that  $R$  and  $L$  do not depend on the standoff distance when the coupling factor  $k$  changes [15].

Further, from Eq. (1), the resonance frequency can be obtained from the denominator:

$$f_{\text{resonance}} = \frac{1}{2\pi} \sqrt{\frac{R_1(R_0 + R_2)}{L_1L_2 - M^2}} = \frac{1}{2\pi} \sqrt{\frac{R_1(R_0 + R_2)}{(1 - k^2)L_1L_2}} \quad (2)$$

#### 4.1. Empirical expression for the coupling coefficient

From the detection exercise of the subsurface grooves, it has been shown that the sensitivity decreases as the depth from the sample's surface increases. An exponential trend showing the variation of  $|S_{21}|$  with respect to the standoff distance is presented in Fig.7. It was demonstrated that the sensor was also sensitive to the electrical conductivity of the panel [10]. At higher frequencies, the sensitivity decreased as the conductivity of the CFRP panel increased. Therefore, standoff distance ( $s$ ), subsurface depth ( $h$ ) and conductivity ( $\sigma$ ) of the sample are taken into account, as shown in Fig.10.

The exponential decay function is introduced here for the description of the coupling coefficient based on the observations, which is written as:

$$k = k_{\text{air}}[(1-\alpha)\beta(\gamma-1)+1] \quad (3)$$

Where

$$\left. \begin{aligned} \alpha &= e^{-C_1 \frac{h}{h_{\text{max}}}} = e^{-C_1 h \sqrt{\pi f \mu \sigma}} \\ \beta &= e^{-C_2 s} \\ \gamma &= e^{-C_3 \sigma} \end{aligned} \right\} \quad (4)$$

$\alpha$ ,  $\beta$  and  $\gamma$  are the coefficients considering the effects of  $h$ ,  $s$  and  $\sigma$ , respectively.  $C_1$ ,  $C_2$  and  $C_3$  are three exponential decay constants. The computation of these three constants will be demonstrated in the next section. The variable,  $h_{\text{max}}$ , is the maximum penetration depth of the electromagnetic waves into conductive materials, which is defined as [14]:

$$h_{\text{max}} = \sqrt{\frac{2}{w\mu\sigma}} = \frac{1}{\sqrt{\pi f \mu \sigma}} \quad (5)$$

Where  $\mu$  is the magnetic permeability of the material. Here, the magnetic permeability  $\mu$  of the carbon fibre composite material is equal to that of the free space  $\mu_0$  (i.e.  $4\pi \times 10^{-7} \text{ H} \cdot \text{m}^{-1}$ ), as the CFRP is nonmagnetic.

#### 4.2. Constant setting

##### a) Setting for the equivalent circuit model

In the present case, due to symmetry, the resistance and inductance of the feed coil are equal to those of the detector coil, i.e.,  $R_1=R_2$ , and  $L_1=L_2$ , respectively. Referring to the formulae in [16], the inductance of the planar spiral square coil is calculated, that is,  $L_1=L_2=123 \text{ nH}$ . The experimental results presented in the section of the parametric study are utilised to compute two unknown parameters, i.e.  $R$  and  $k$ . By the brute-force algorithm, the combination of  $R = 31.75 \Omega$  and  $k=0.24$  is found to give the best fit to the experimental results. Furthermore,  $k=0.31$  is found to be capable of simulating the case where the sensor is placed in the air.

In this case, the calculated resonance frequency is 69 MHz, which agrees well with the experiment (i.e. 71.88 MHz). As illustrated in Fig.11, the results from the analysis of the equivalent circuit modelling agree well with the experimental data.

#### b) Setting for the empirical expression of k

The values of three exponential decay constants,  $C_1=3.8$ ,  $C_2=0.8$ , and  $C_3=0.128$ , are determined based on the experimental results. For the contact case with no damage underneath, the factor  $\alpha$  is cancelled and  $g=0$ . Hence, Eq. (4) becomes

$$k_{\text{contact}} = \gamma k_{\text{air}} = e^{-C_3 \sigma} k_{\text{air}} \quad (7)$$

So, the constant  $C_3$  can be computed by substituting the conductivity of the panel, and the coupling constants  $k_{\text{air}}$  and  $k_{\text{contact}}$ .

$$C_3 = -\frac{\ln(k_{\text{contact}}/k_{\text{air}})}{\sigma} \quad (8)$$

For the calculation of  $C_3$ , the measurement of the electrical conductivity of the sample is required. It is known that the electrical conductivity of the CFRP is anisotropic [17]. For a unidirectional lamina, the longitudinal conductivity is significantly larger than the transverse conductivity [18]. Hence, the currents induced in the external coupling process mainly flow along the carbon fibres. The average longitudinal conductivity for calculation is measured, which is 2289 S/m.

#### 4.3. Prediction of the maximal detection depth

In this section, the proposed model is applied for the prediction of the maximum detection depth for a fixed standoff distance. As shown in Fig.12, the sensitivity values at different subsurface depths are obtained by modelling, and a linear line is also obtained by using the regression analysis. The maximum detection depth predicted by the modelling agrees well with that by the experiment, which demonstrates the accuracy of the proposed empirical expression for the coupling coefficient.

## 5. Further sensor development for sensitivity improvement

### 5.1. Attachment of the ferrite sheet

The previous experiments and modelling demonstrated that the maximum detection depth for a typical setup is limited to around 1.85 mm. In order to improve the sensitivity and penetration depth, ferrite layers were added to the sensor to reduce the reluctance of the coupled magnetic circuit. A ferrite sheet (IRJ04®) of dimension 20.0 mm × 7.0 mm × 0.25 mm and  $\mu_r = 40$  was introduced to the upper side of the CSI sensor.

A line scanning is conducted to detect the first groove underneath the same CFRP strip shown in Fig.3. The effect of the number of the ferrite layers is also studied. As presented in Fig.13, compared with the original CSI, the sensitivity provided by the added ferrite is improved. It is shown that the measurement results obtained from the sensor with three ferrite layers could provide better sensitivity improvement than other two ferrite cases. As the noise level is within 0.1 dB, the results show that the SNR value in the case with the introduced ferrite is increased by approximately 22% compared with that obtained by the original Salski CSI configuration.

### 5.2. The yoke sensor

#### 5.2.1. Methodology

In the previous section, ferrite layers improved the sensitivity of the CSI sensor. A ferrite yoke arrangement schematically shown in Fig. 14 was constructed and applied. The yoke sensor consists of two coils and ferrite pieces. Each coil is made up of 30 turns of the shellac coated copper wire with a diameter of 220  $\mu\text{m}$ . The whole sensor is mounted on the same substrate as the CSI sensor. The epoxy adhesive is used to glue each component together, such as the interfaces between the cylindrical ferrite cores and the flat ferrite sheet, the interface between the ferrite sheet and the surface of the substrate. Then the leads from the two coils are soldered to two SMA connectors.

### 5.2.2. Sensitivity comparison

#### *a) Detection of subsurface grooves*

For comparison, the yoke sensor is used to scan across the composite strip containing the six machined grooves. The CSI sensor with three ferrite layers is also employed. The performances of the sensors at the same frequency  $f=10$  MHz are studied. As presented in Fig.15, the six grooves can be accurately picked up by three sensors. Specifically, the curves for two CSI cases (with and without Ferrite patch) are similar, while the yoke sensor provides the highest sensitivity.

The relationship between the subsurface depth and the average magnitude of Stage II in three cases are shown in Fig.16. The regression analysis is also performed for sensitivity analysis. The linear relationship can also be found in the yoke sensor. It is demonstrated that the yoke sensor is more sensitive to shallower defects. For example, for the third groove with the subsurface depth of 0.80 mm, the sensitivity provided by the Salski CSI sensor is 1.27 dB, while that obtained by the yoke sensor is 2.00 dB, which shows the signal-to-noise ratio (SNR) is improved by around 57%.

#### *b) Detection of simulated delamination*

When composites are loaded in bending or under lateral impact, delamination (separation of neighbouring layers) can occur and this can be difficult to detect since it happens internally. Here an air gap measurement set-up is arranged to demonstrate the potential detection of delamination using the newly developed sensor. Delamination is simulated by partially filling the machined grooves with small fillers of the same width 4.00 mm, creating an air gap (simulated delamination), as shown in Fig. 17.

The size of the air gap is 0.82 mm and 0.34 mm, respectively. The line scanning is conducted across each groove at a standoff distance of  $250\text{ }\mu\text{m}$  and an operating frequency 8 MHz. Fig.18 shows the comparison of the sensitivity curve provided by the CSI sensor and the yoke sensor operated at the same frequency. In both cases, the sensitivity of the yoke sensor is larger than that of the standard

CSI sensor, which demonstrates a useful advantage in practice, especially when impact induced delaminations introduce a much smaller ply separation (air gap).

In Fig.19 some preliminary results are presented for a 2D plain weave carbon fibre-epoxy laminate loaded in three-point bending. A long noticeable delamination can be seen in Fig.19 (a). A line scanning is conducted with a standoff distance of  $250\text{ }\mu\text{m}$  and step size of  $126.7\text{ }\mu\text{m}$ . As shown in Fig.19 (b), the performance of the sensor at 5 MHz is tested and the crack is clearly identified. The trend of the curve agrees with the three-stage analysis by the previous study, see Fig.4. The measured length of the crack at the edge of the sample is 4.98 mm, compared to 4.7mm obtained by the MATLAB code developed for the sensor data extraction, giving confidence to the proposed electromagnetic based non-contact sensing system.

## 6. Concluding remarks

In this work, the electromagnetic CSI sensor has been successfully employed for damage detection and evaluation in CFRP composites. From the detection of subsurface grooves, it has been found that the width, location and depth of the groove can be easily obtained from the 3-stage analysis of the sensitivity curve. A linear relationship between the average magnitude of the second stage in the sensitivity curve and the subsurface depths of the grooves have been revealed. In addition, the sensor has been employed to the detection of the real impact and three-point bending induced damage on a CFRP composite plate. The generated images strongly suggested the presence, location and extent of the induced damage.

The parametric study that has been conducted to investigate the effects of the inspection frequency, the stand-off distance and the signal power on the performance has revealed that the sensitivity declines as the separation of the sensor and the top surface increases; the sensor's performance is independent of the signal power.



1 An equivalent lumped circuit model for the EM sensor has been proposed considering the effects of  
2  
3 the stand-off distance, the subsurface depth and the conductivity. A good agreement with the  
4  
5 experimental measurements is observed, which suggests that the analytical model could provide a  
6  
7 practical tool for performance prediction and optimal design.  
8  
9

10 Two scenarios for the sensitivity improvement using ferrite material are provided. First, the ferrite  
11  
12 sheet is attached on the top side of the CSI sensor for the concentration of the magnetic field. The  
13  
14 results show that the introduction of the ferrite sheet contributes to the improvement of the  
15  
16 performance. Second, a yoke sensor with ferrite and encircling coils is designed. It has been shown  
17  
18 that the SNR parameter provided by the latter sensor is improved by 57%, which is considered as  
19  
20 significant in the effort to identify impact induced damage in multi-layered composite plates. Further  
21  
22 work is required to investigate the ability of the proposed sensor in identifying multiple, overlapping  
23  
24 delaminations; these results will be reported in near future publications.  
25  
26  
27  
28  
29  
30  
31

## 32 **Acknowledgement**

33  
34 This work was funded by Dean's Doctoral Scholar award, School of Materials, The University of  
35  
36 Manchester. The authors would like to thank Mohamed Saleh for providing composite samples  
37  
38 essential for the experiments and Drs Edward McCarthy and Matthieu Gresil from School of  
39  
40 materials for many useful discussions. Thanks also to Professor Prasad Potluri for his guidance and  
41  
42 assistance. The first author gratefully acknowledges valuable discussions with Bartlomiej Salski.  
43  
44  
45  
46  
47  
48

## 49 **References**

- 50  
51  
52 [1] Soutis C. Carbon fiber reinforced plastics in aircraft construction. Mater Sci Eng A  
53  
54 2005;412:171–6.  
55  
56  
57  
58  
59  
60  
61  
62  
63  
64  
65

- [2] Giurgiutiu V, Soutis C. Enhanced composites integrity through structural health monitoring. *Appl Compos Mater* 2012;19:813–29.
- [3] Pavlopoulou S, Worden K, Soutis C. Structural health monitoring and damage prognosis in composite repaired structures through the excitation of guided ultrasonic waves. *SPIE Smart Struct. Mater. Eval. Heal. Monit.*, International Society for Optics and Photonics; 2013, p. 869504–869504.
- [4] Yin W, Withers PJ, Sharma U, Peyton AJ. Noncontact characterization of carbon-fiber-reinforced plastics using multifrequency eddy current sensors. *IEEE Trans Instrum Meas* 2009;58:738–43.
- [5] Caminero M, Pavlopoulou S, Lopez-Pedrosa M, Nicolaisson BG, Pinna C, Soutis C. Using digital image correlation techniques for damage detection on adhesively bonded composite repairs. *Adv Compos Lett* 2012;21:51–7.
- [6] Diamanti K, Hodgkinson JM, Soutis C. Detection of low-velocity impact damage in composite plates using Lamb waves. *Struct Heal Monit* 2004;3:33–41.
- [7] Valiente LA, Haigh AD, Gibson AAP, Parkinson G, Jacobs G, Withers PJ, et al. Coplanar waveguide scanning microwave profiler. 2007 *Eur. Microw. Conf.*, IEEE; 2007, p. 194–7.
- [8] Li Z, Haigh A, Soutis C, Gibson A. Simulation for the impact damage detection in composites by using the near-field microwave waveguide imaging. 53rd *Annu. Conf. Br. Inst. Non-Destructive Test.*, Manchester, UK: 2014.
- [9] Blitz J. *Electrical and magnetic methods of non-destructive testing*. Springer Science & Business Media; 1997.
- [10] Salski B, Gwarek W, Korpas P. Electromagnetic inspection of carbon-fiber-reinforced polymer composites with coupled spiral inductors. *IEEE Trans Microw Theory Tech* 2014;62:1535–44.

- [11] Salski B, Gwarek W, Korpas P. Non-destructive testing of carbon-fiber-reinforced polymer composites with coupled spiral inductors. 2014 IEEE MTT-S Int. Microw. Symp., IEEE; 2014, p. 1–4.
- [12] Salski B, Gwarek W, Korpas P, Reszewicz S, Chong AYB, Theodorakeas P, et al. Non-destructive testing of carbon-fibre-reinforced polymer materials with a radio-frequency inductive sensor. *Compos Struct* 2015;122:104–22.
- [13] Li Z, Haigh A, Soutis C, Gibson A, Sloan R, Karimian N. Damage evaluation of carbon-fibre reinforced polymer composites using electromagnetic coupled spiral inductors. *Adv Compos Lett* 2015;24:44–7.
- [14] Pozar D. *Microwave engineering*. Fourth edi. New York: John Wiley & Sons; 2009.
- [15] García-Martín J, Gómez-Gil J, Vázquez-Sánchez E. Non-destructive techniques based on eddy current testing. *Sensors* 2011;11:2525–65.
- [16] Mohan SS, del Mar Hershenson M, Boyd SP, Lee TH. Simple accurate expressions for planar spiral inductances. *IEEE J Solid-State Circuits* 1999;34:1419–24.
- [17] Lange R, Mook G. Structural analysis of CFRP using eddy current methods. *NDT E Int* 1994;27:241–8.
- [18] Menana H. Electromagnetic characterization of anisotropic and weakly conductive materials by using resonant circuits. *Prog Electromagn Res Lett* 2014;50:73–7.

Figure captions

**Fig.1.** Schematic diagram of the CSI sensor. (a) Top side (b) Bottom side

**Fig.2.** Schematic diagram of the experimental setup for damage detection by using the CSI sensor

**Fig.3.** Cross section of the CFRP strip with six grooves on the bottom side (not to scale)

**Fig.4.** Analysis of the sensitivity curve obtained from the detection of the six subsurface grooves

**Fig.5.** Relationship between the subsurface depth and the corresponding magnitude of Stage II

**Fig.6.** Parametric study of the effect of the inspection frequency. (a) The sensitivity spectrum at the position above the first groove. (b) Sensitivity curve for the six-groove detection at different frequencies

**Fig.7.** Parametric study of the effect of the standoff distance on the frequency response

**Fig.8.** The distribution of  $|S_{21}|$  obtained by the detection of the BVID on the CFRP sample

**Fig.9.** Diagram of the two-port network in the equivalent circuit modelling for the CSI sensor

**Fig.10.** Three parameters considered in the expression of the coupling coefficient: standoff distance (s), subsurface depth (h) and conductivity ( $\sigma$ ) of the sample

**Fig.11.** Comparison transmission coefficient (i.e.  $|S_{21}|$ ) between the simulation and the experimental measurements in two special cases (i.e. contact and air surrounding, non-contact)

**Fig.12.** Comparison of the sensitivity value with respect to the subsurface depth of the groove

**Fig.13.** Comparison of the sensitivity between the cases with and without the introduced ferrite

**Fig.14.** Schematic diagram of the yoke CSI sensor

**Fig.15.** Comparison of the sensitivity curves between the three sensors for the detection of six subsurface grooves

**Fig.16.** Comparison of the relationship between the subsurface depth and the average magnitude of Stage II obtained by the three sensors

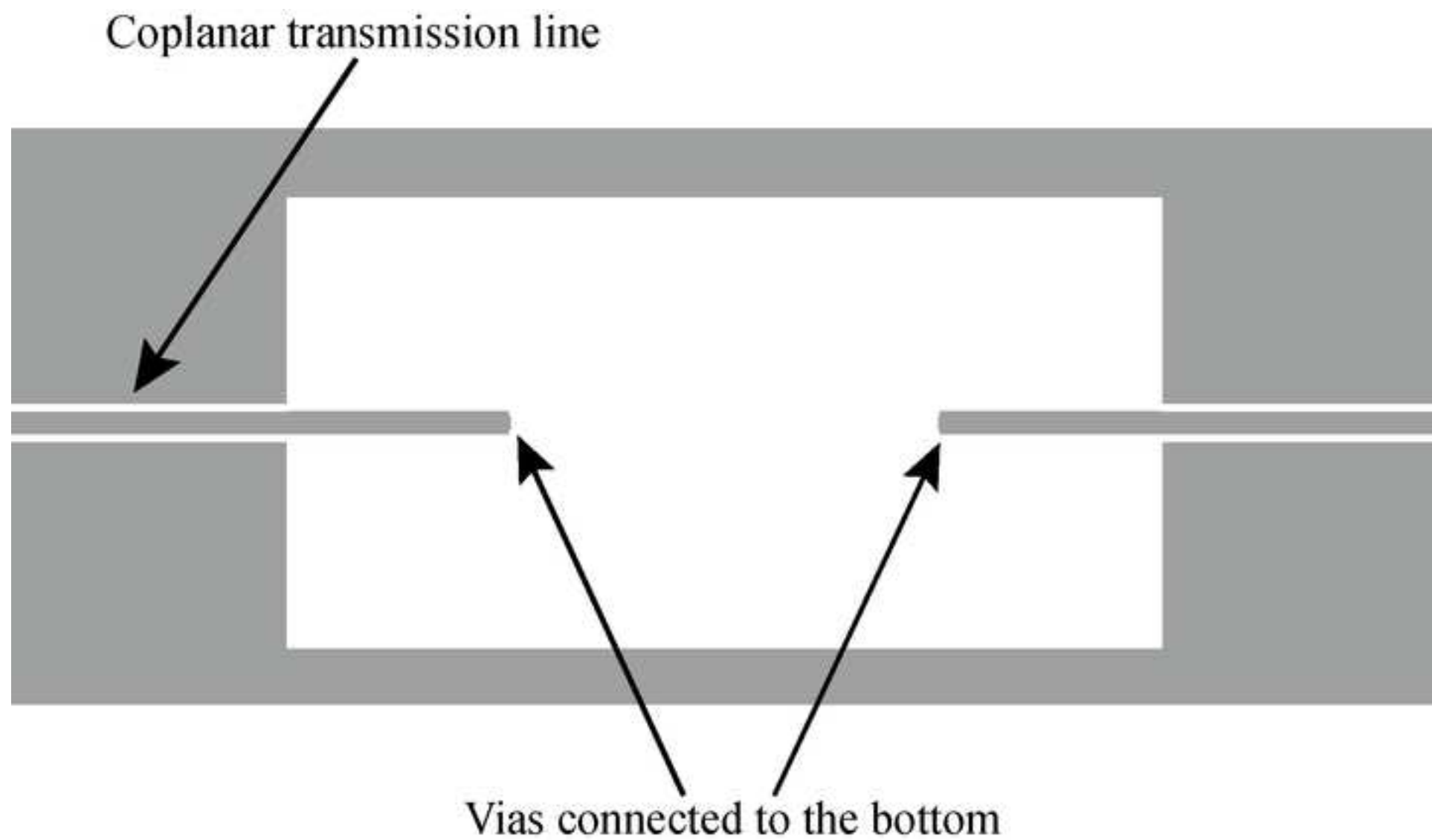
**Fig.17.** Two cases with an artificial delamination created by partially filling the grooves. (a) Case I.  
(b) Case II

**Fig.18.** Comparison of the sensitivity curves for the detection of simulated delamination produced by the CSI sensor and the EM yoke sensor. (a) Case I. (b) Case II

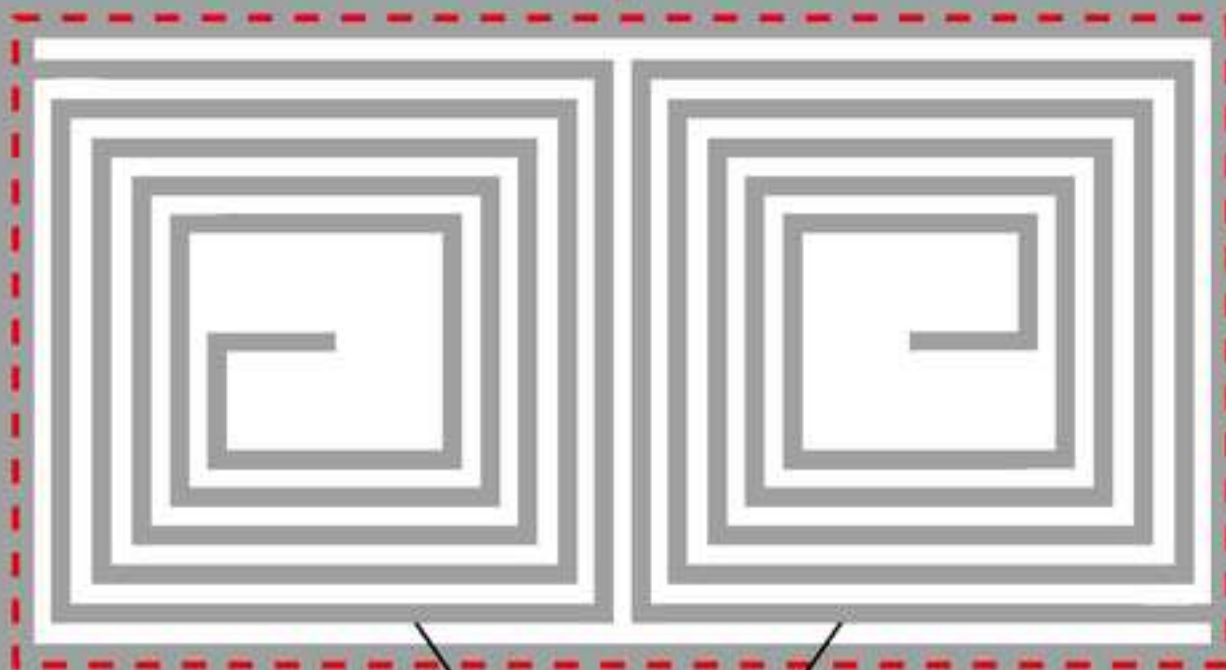
**Fig. 19.** Detection of delamination in a 2D plain woven CFRP sample induced by three-point ending.  
(a) Photograph of the delamination caused by bending. (b) Sensitivity curve

Table caption

Table 1 Summary of the subsurface depths of the grooves and the average magnitude of Stage II in the sensitivity curve



Coupling region



Square spiral inductors

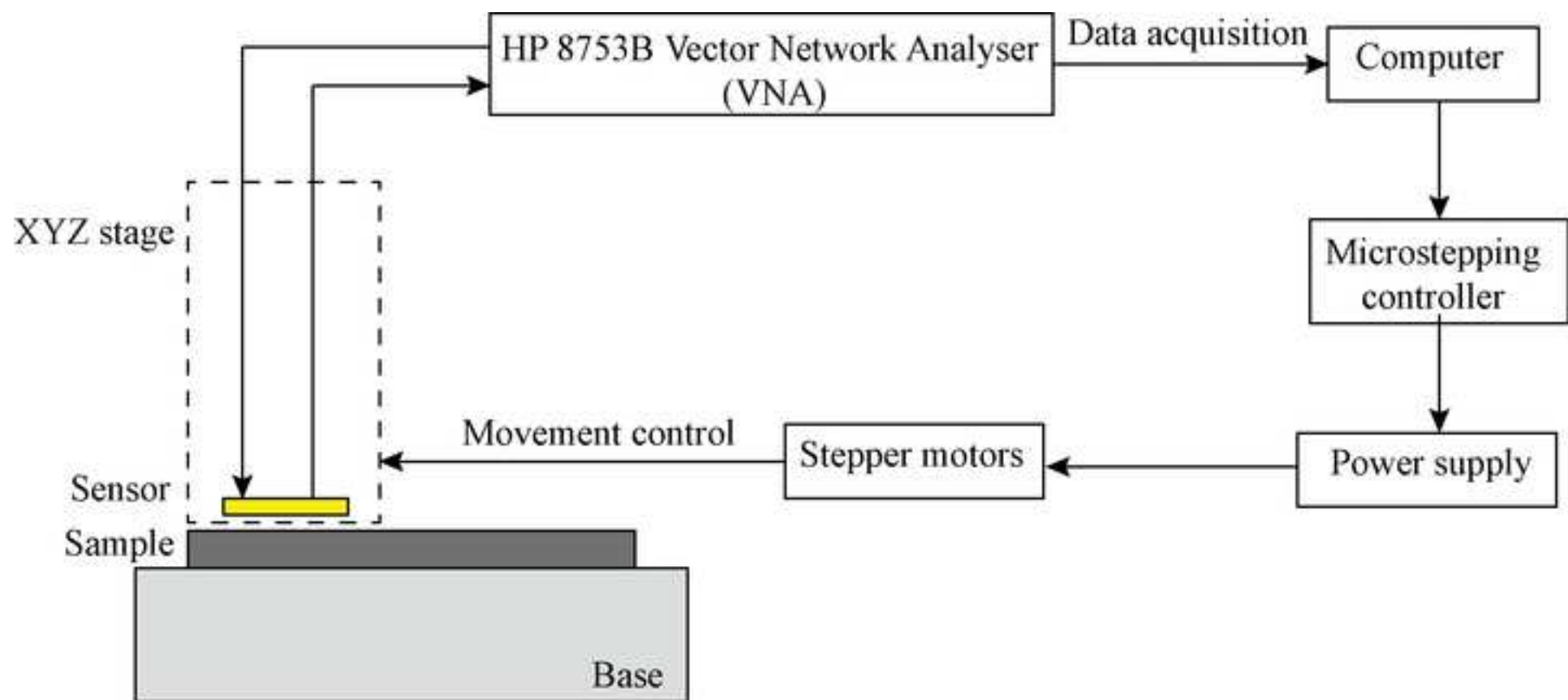
Ground plane





fig2.tif

[Click here to download high resolution image](#)



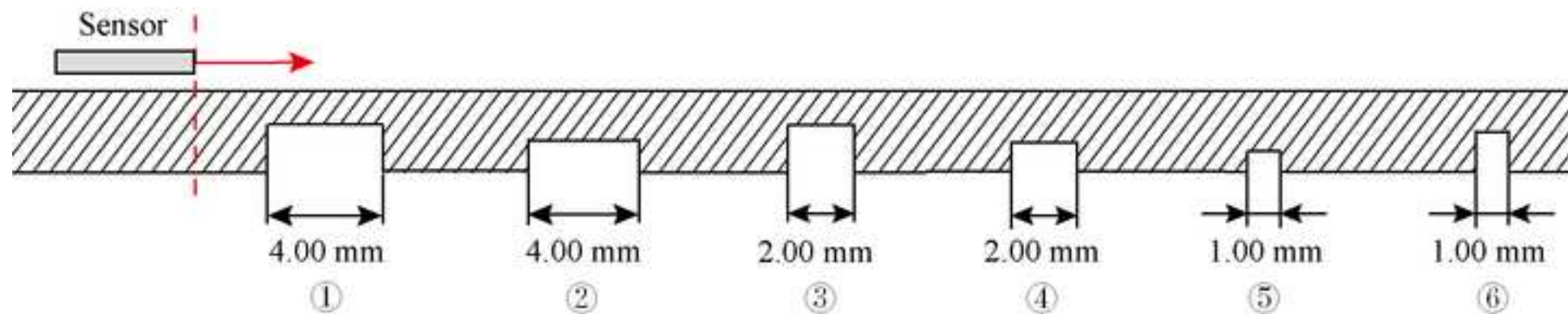
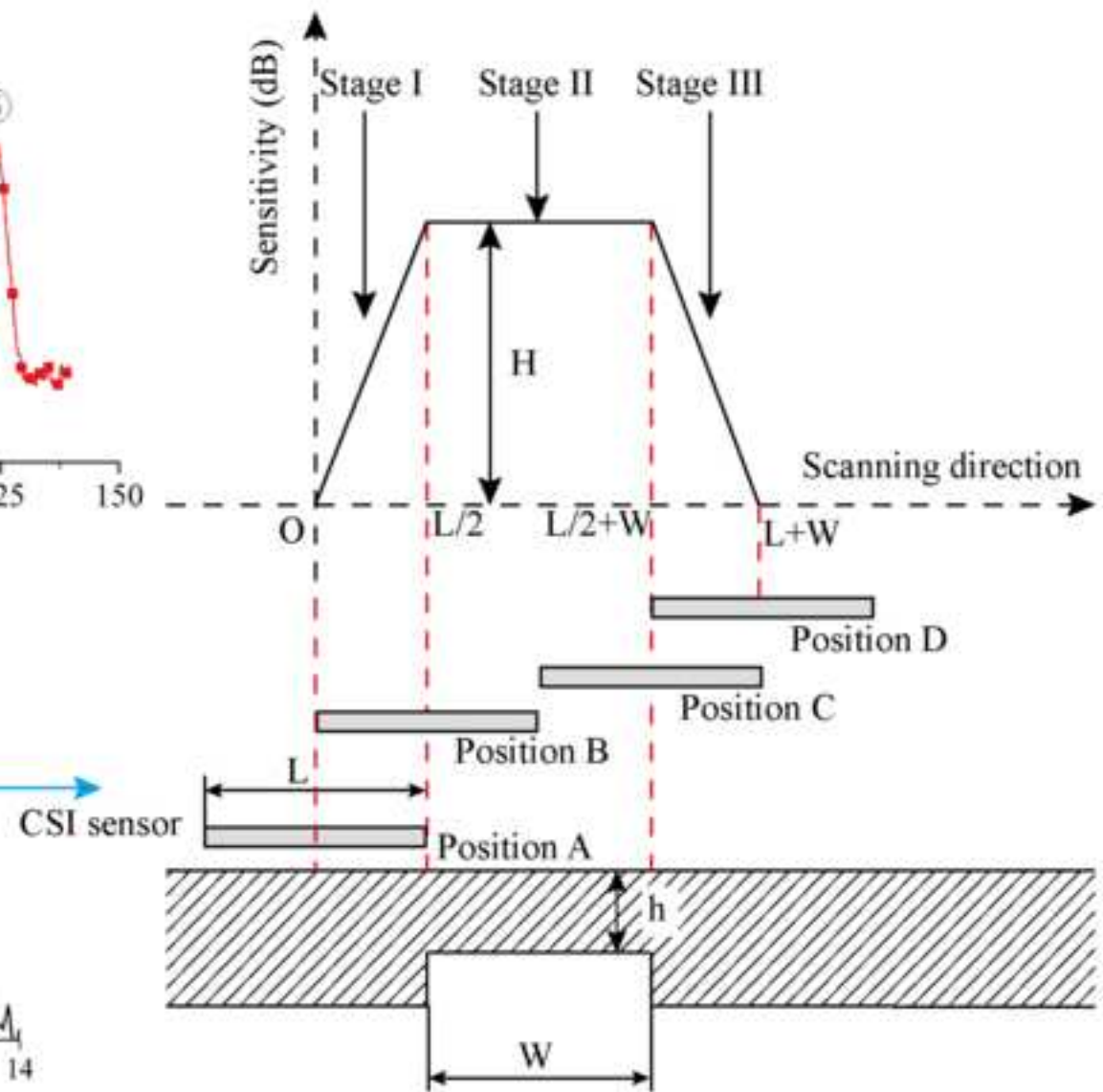
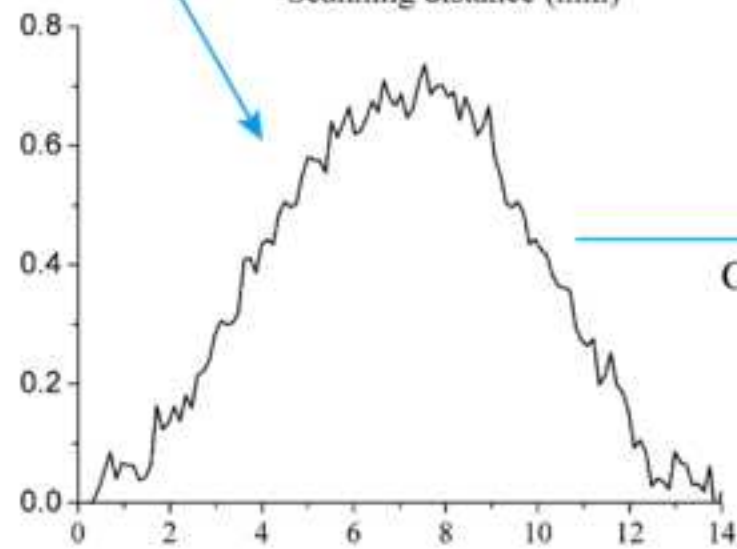
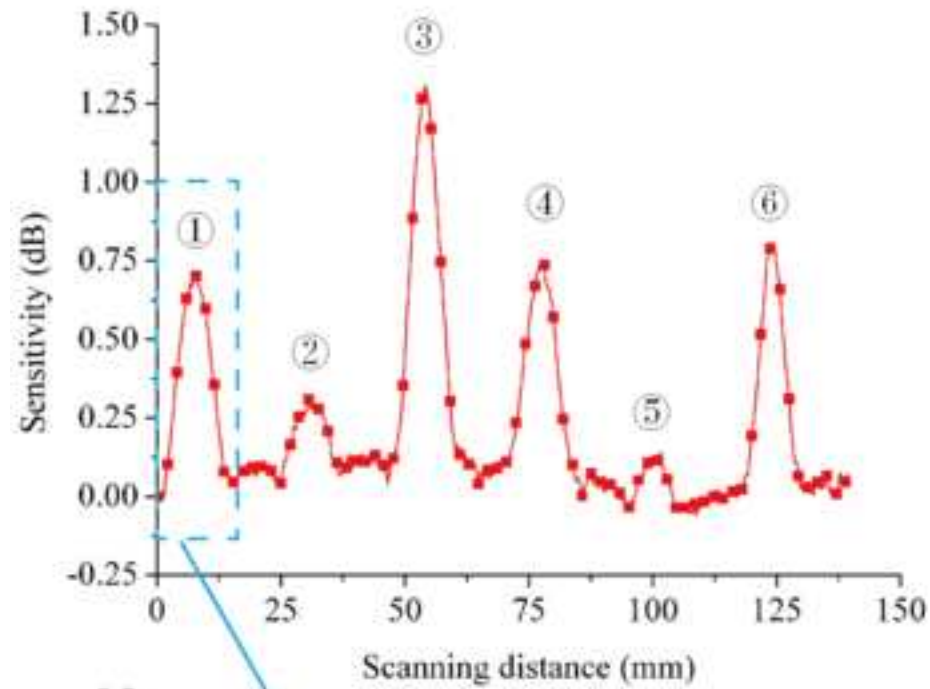
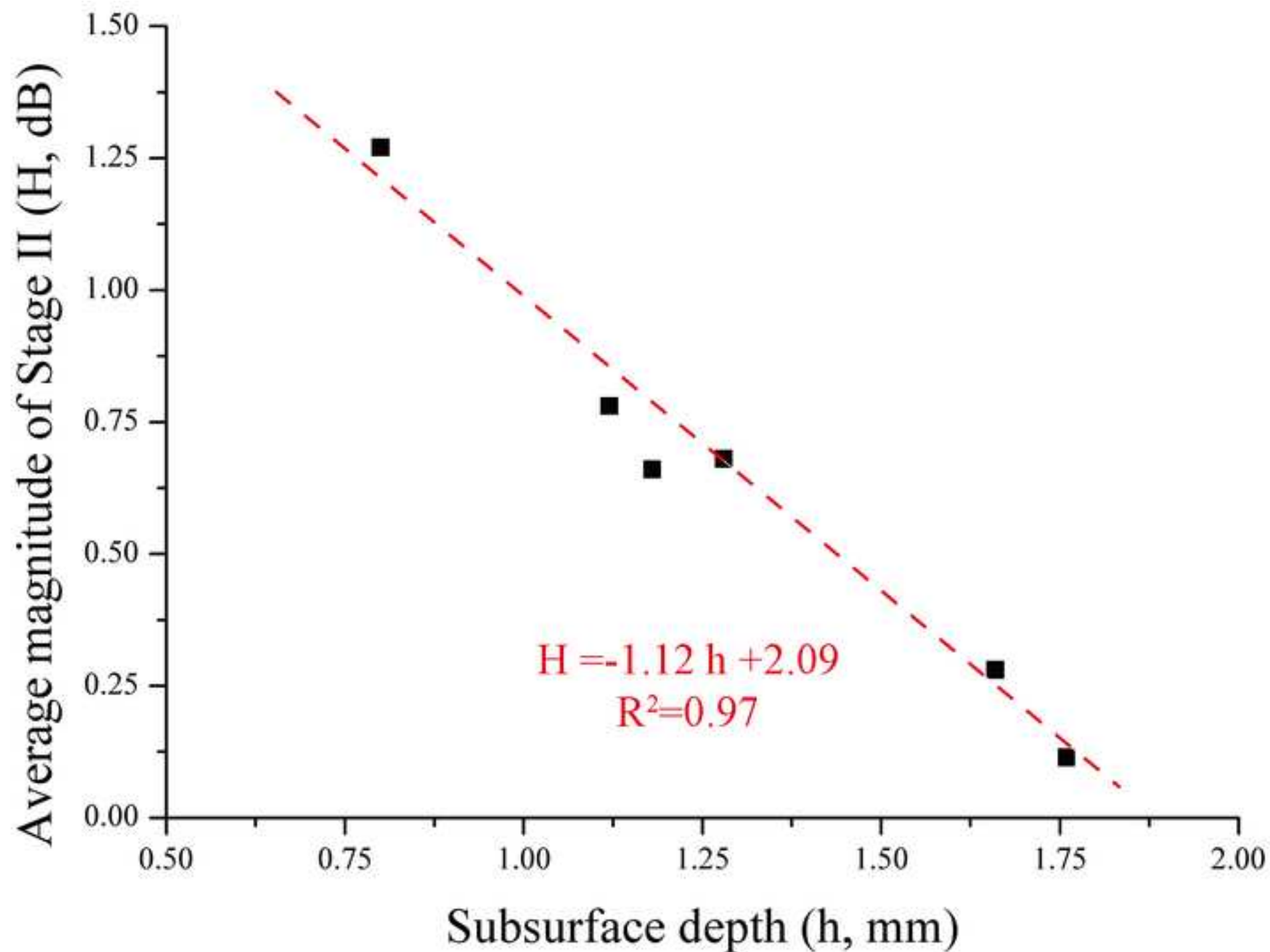
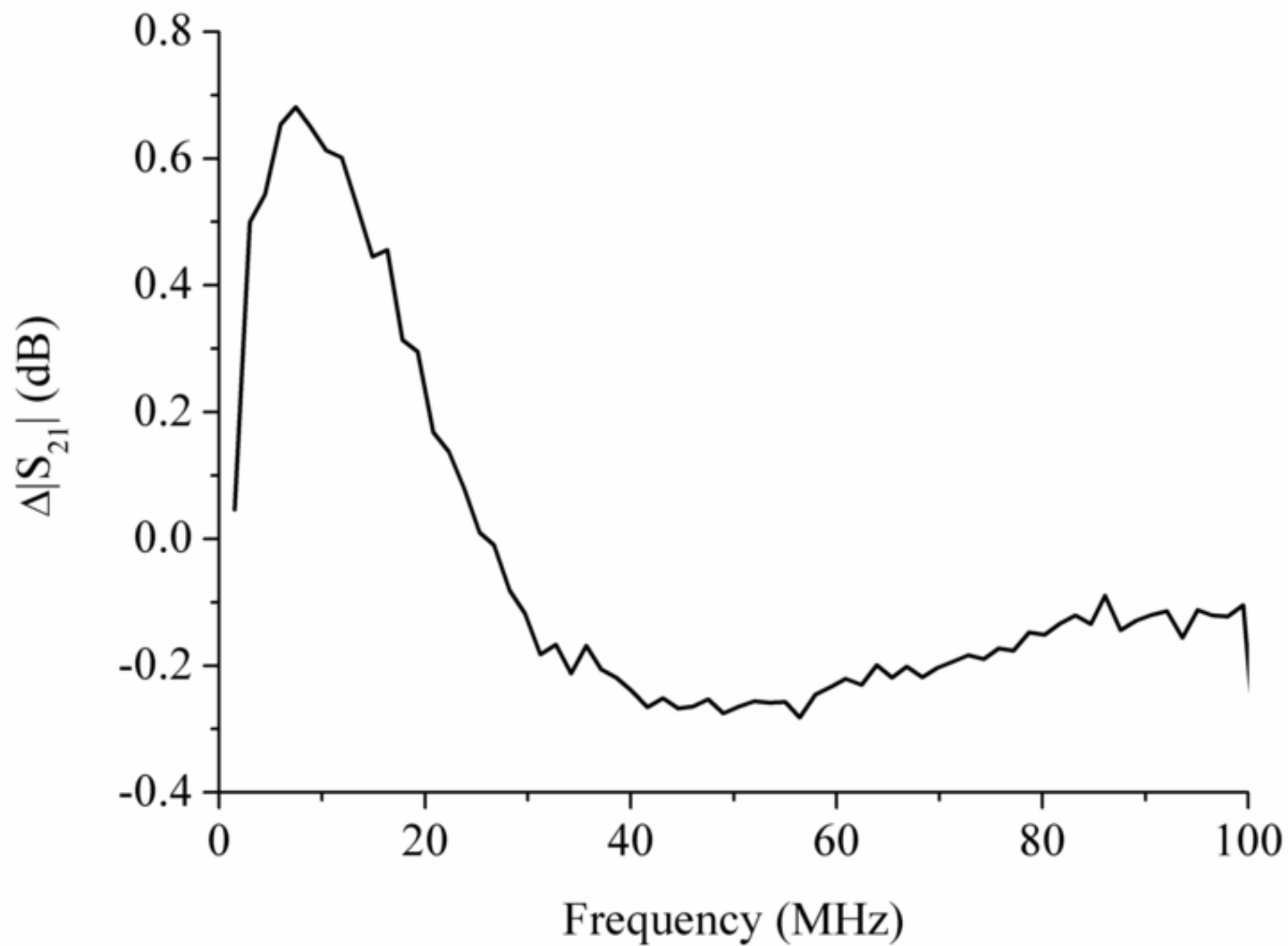


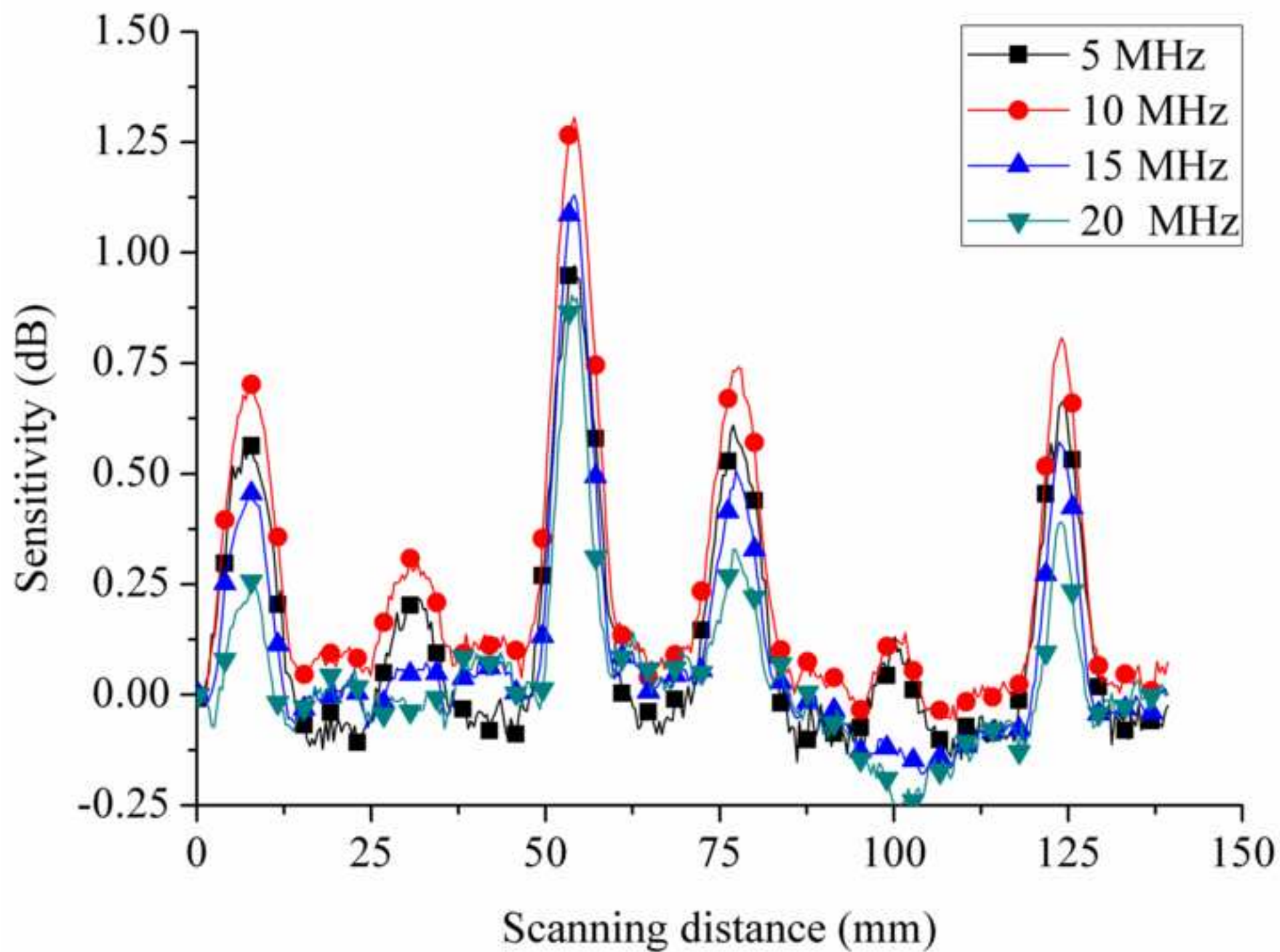
fig4.tif

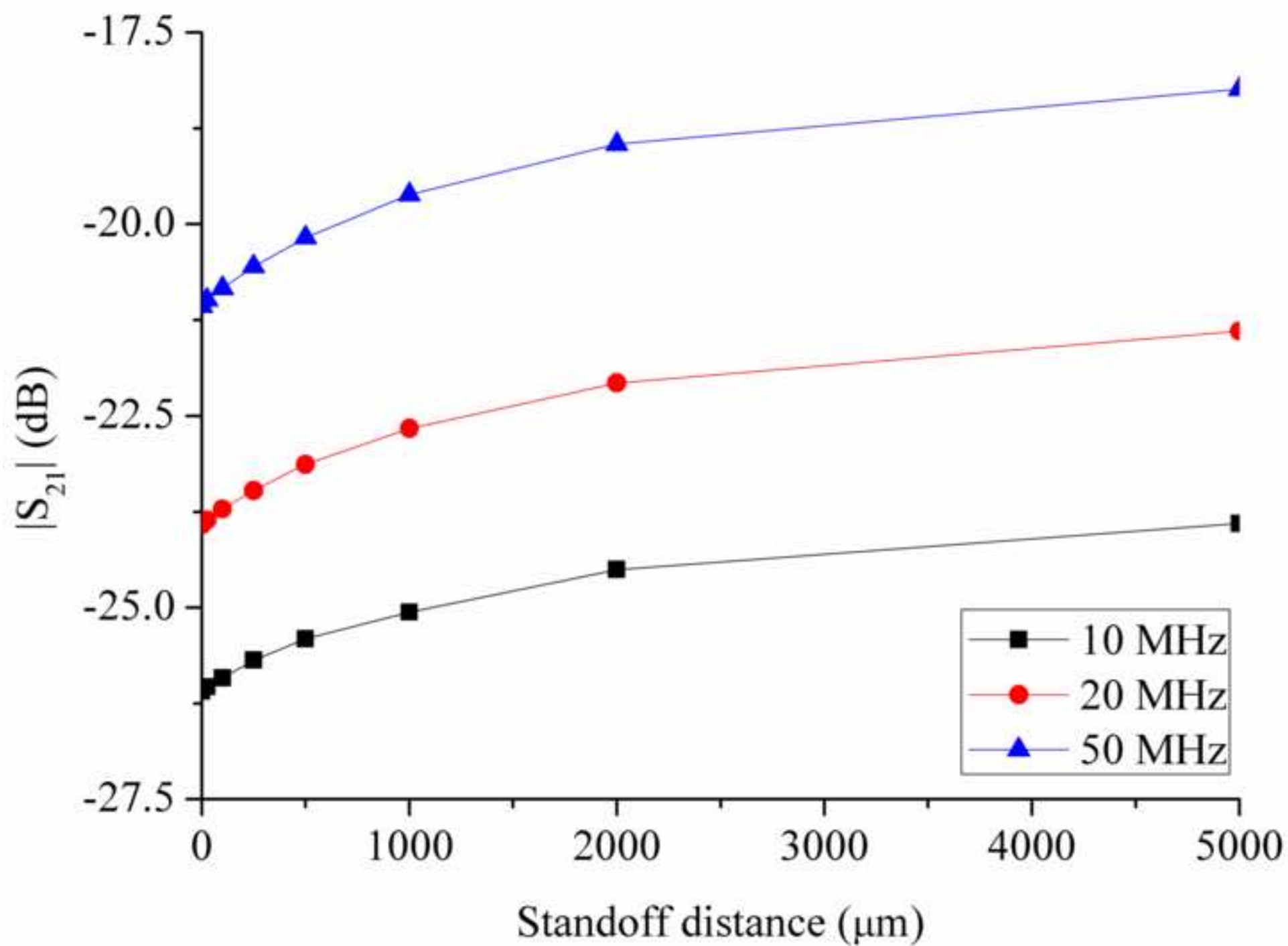
[Click here to download high resolution image](#)



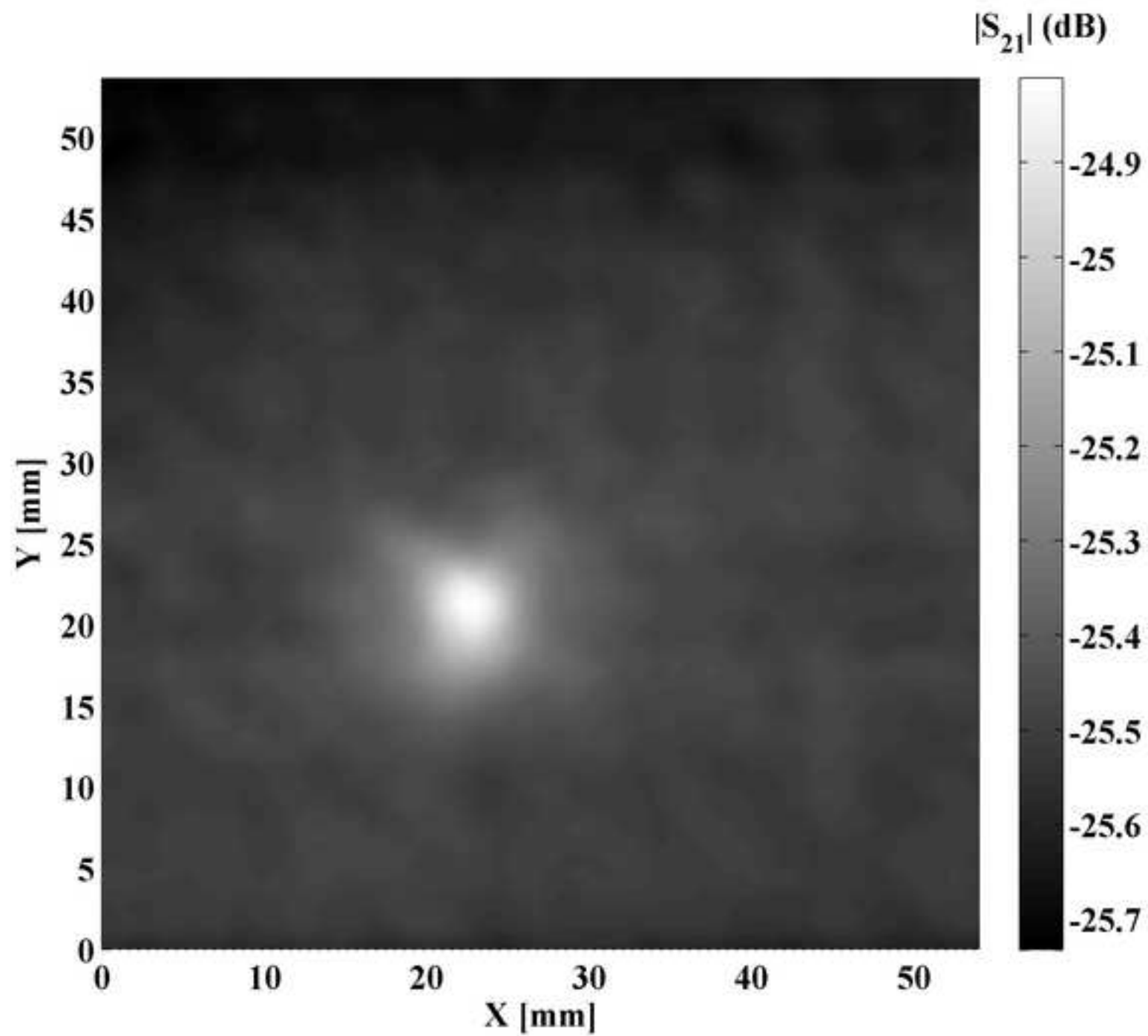




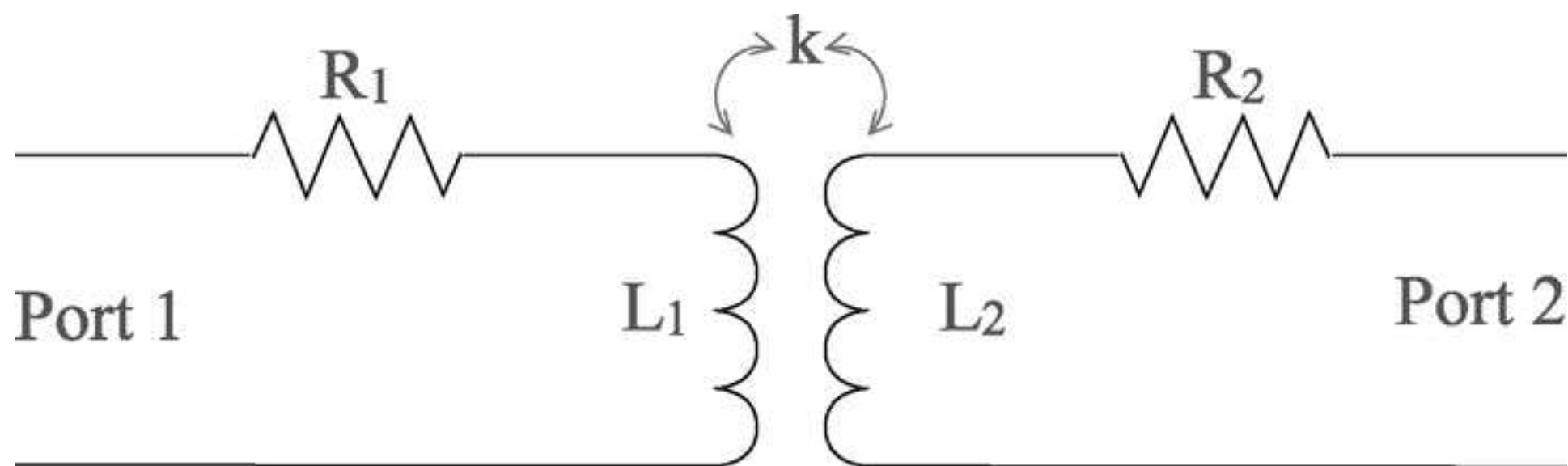


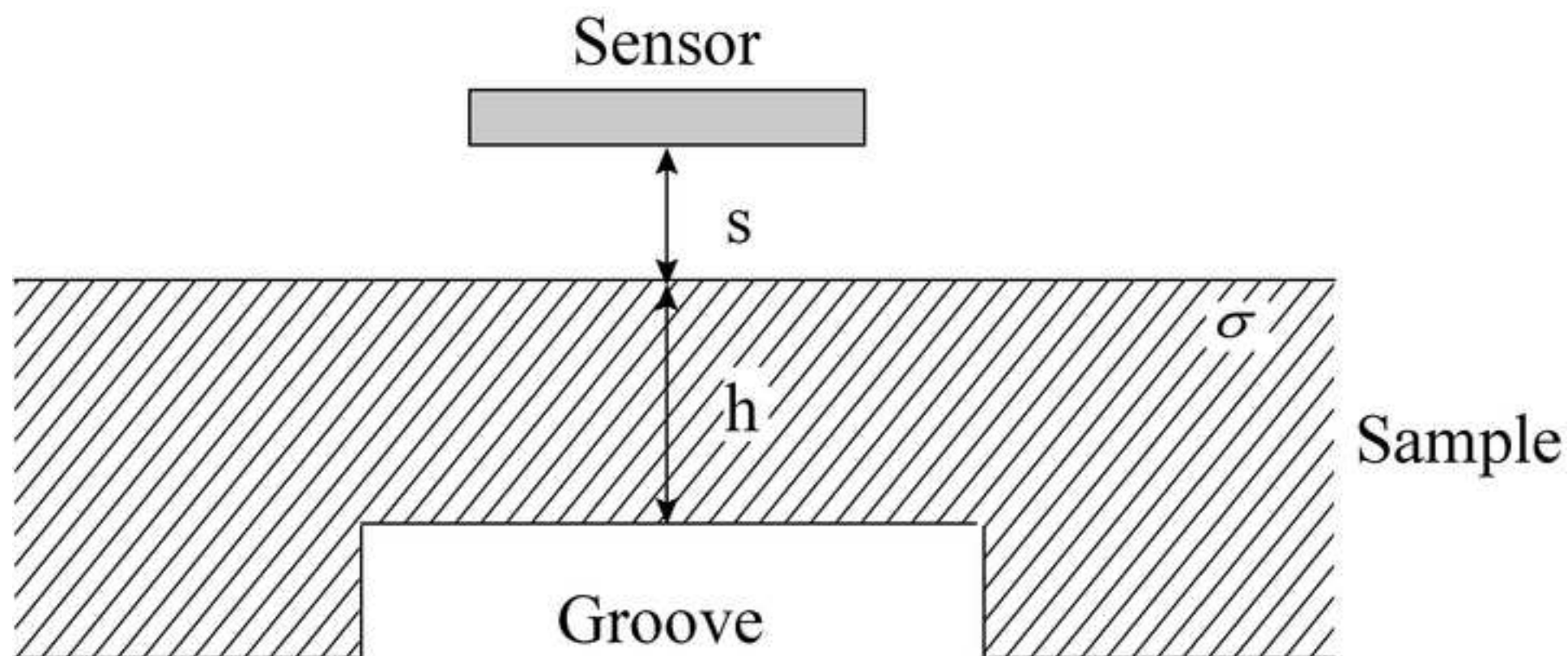


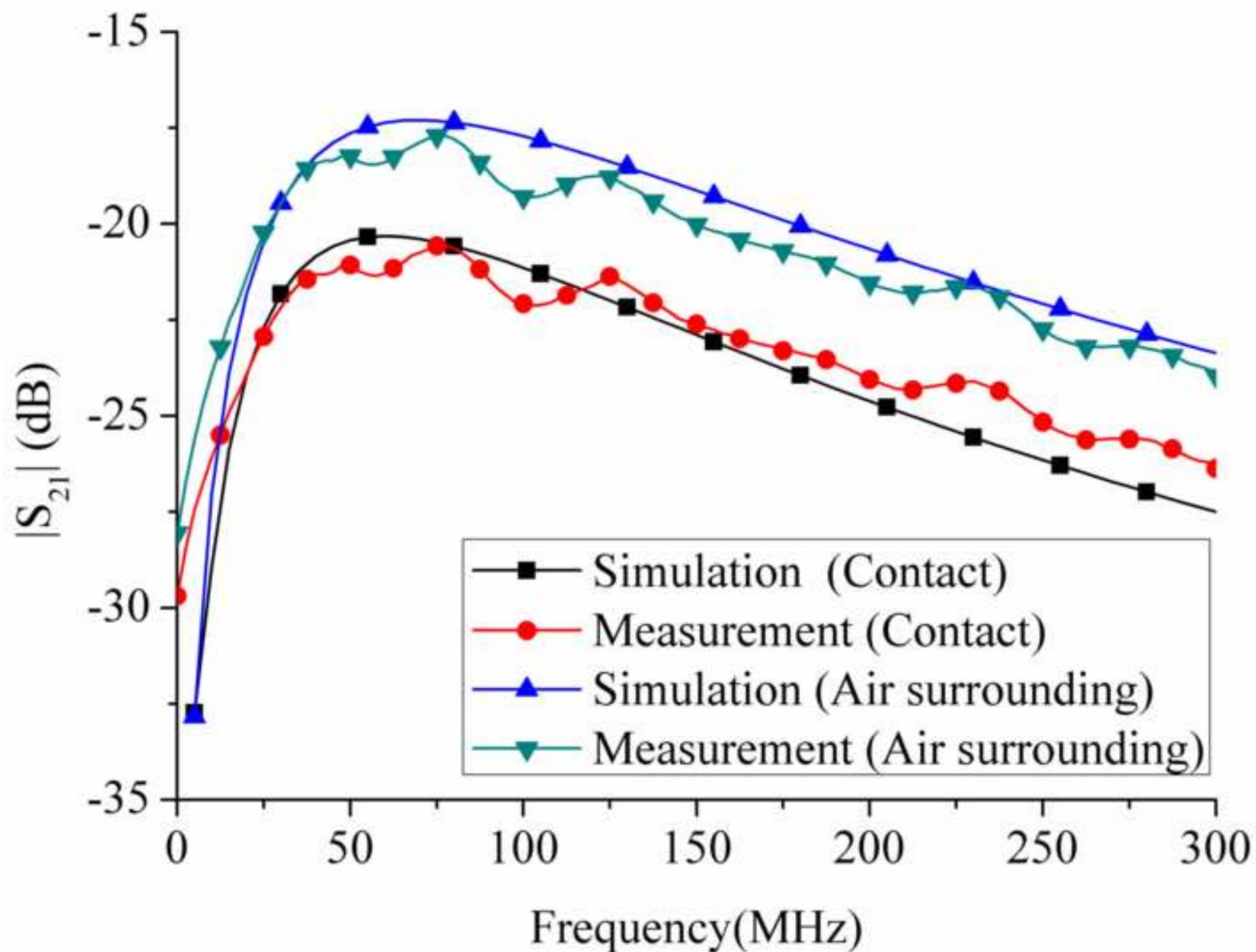


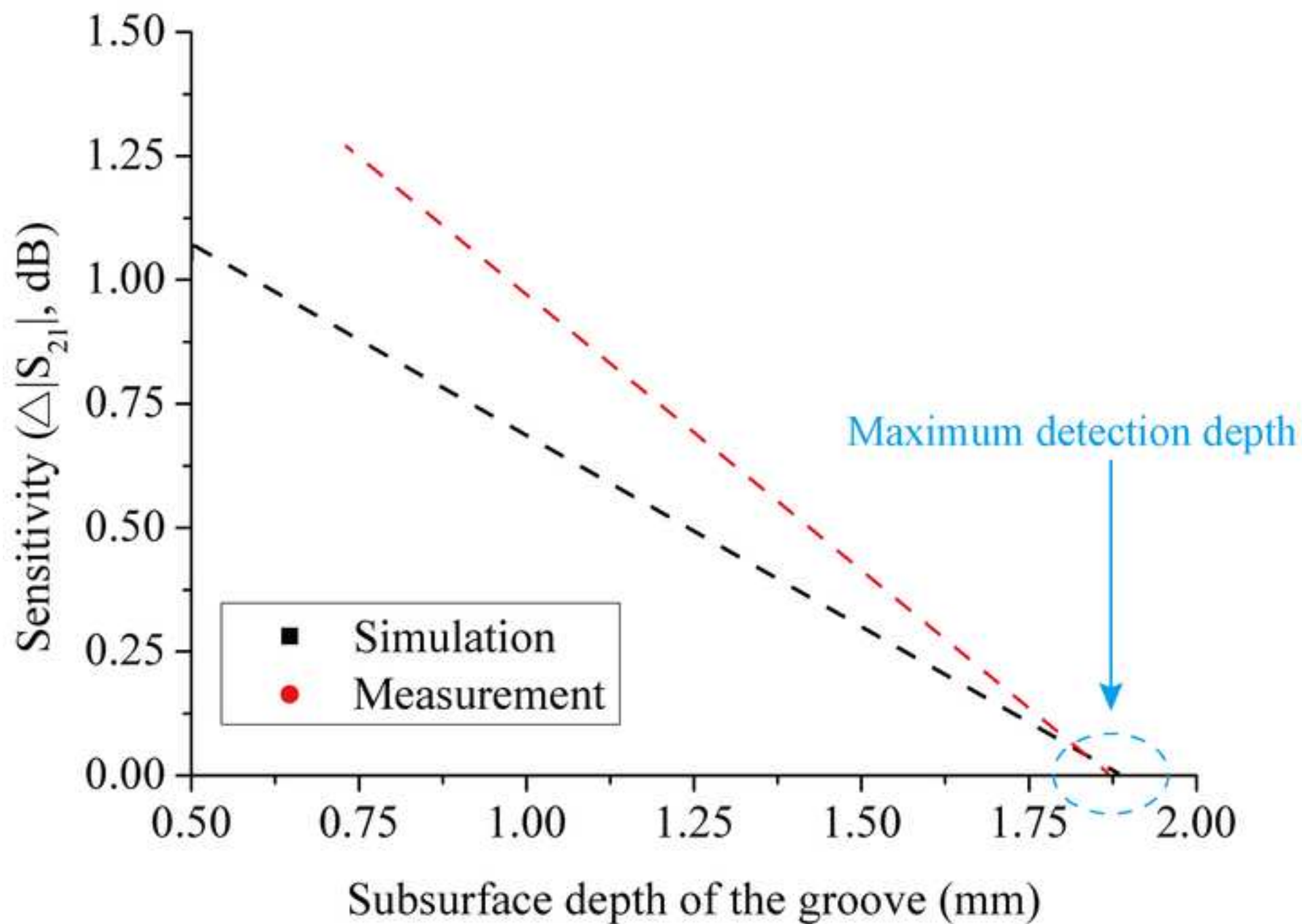












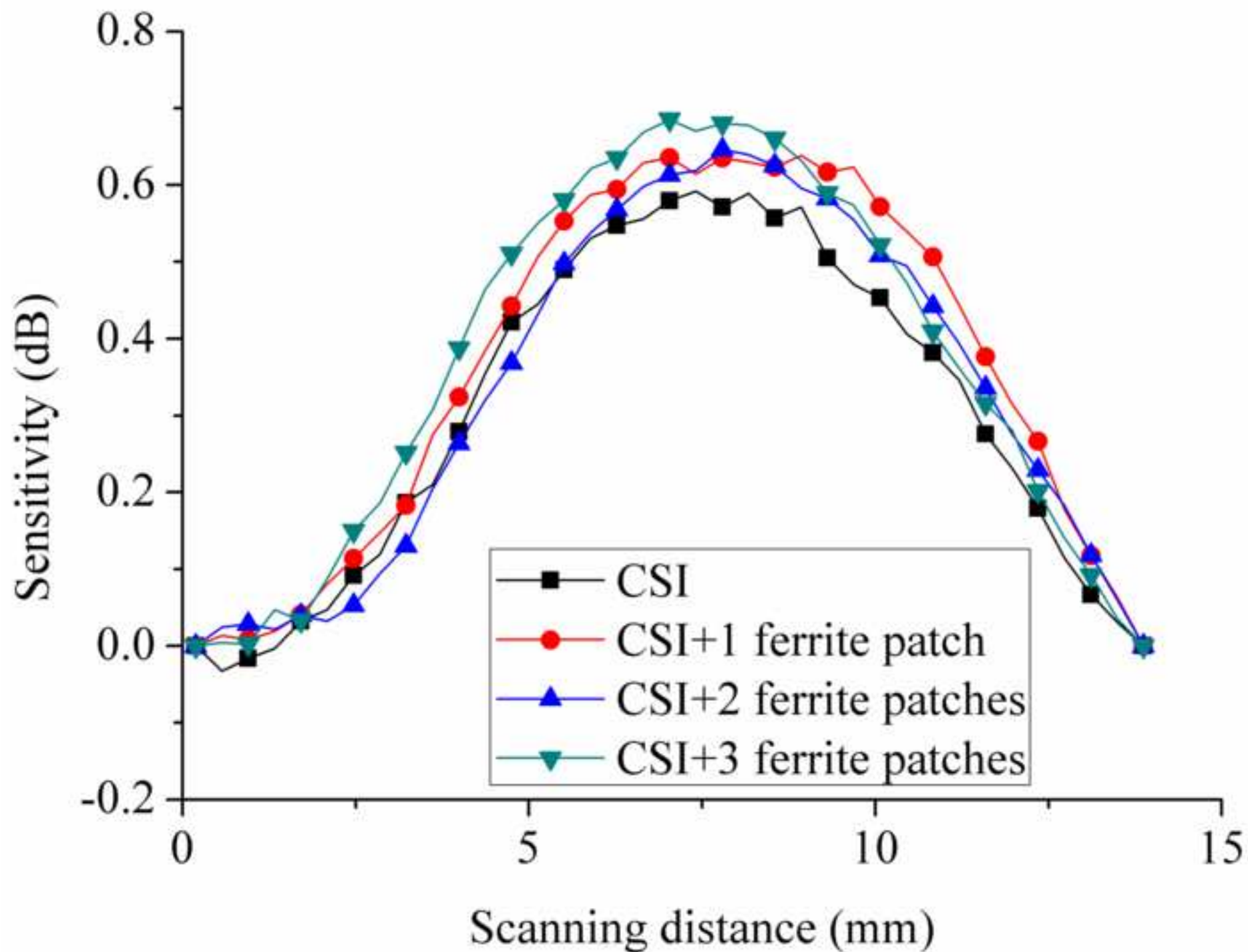


fig14.tif

[Click here to download high resolution image](#)

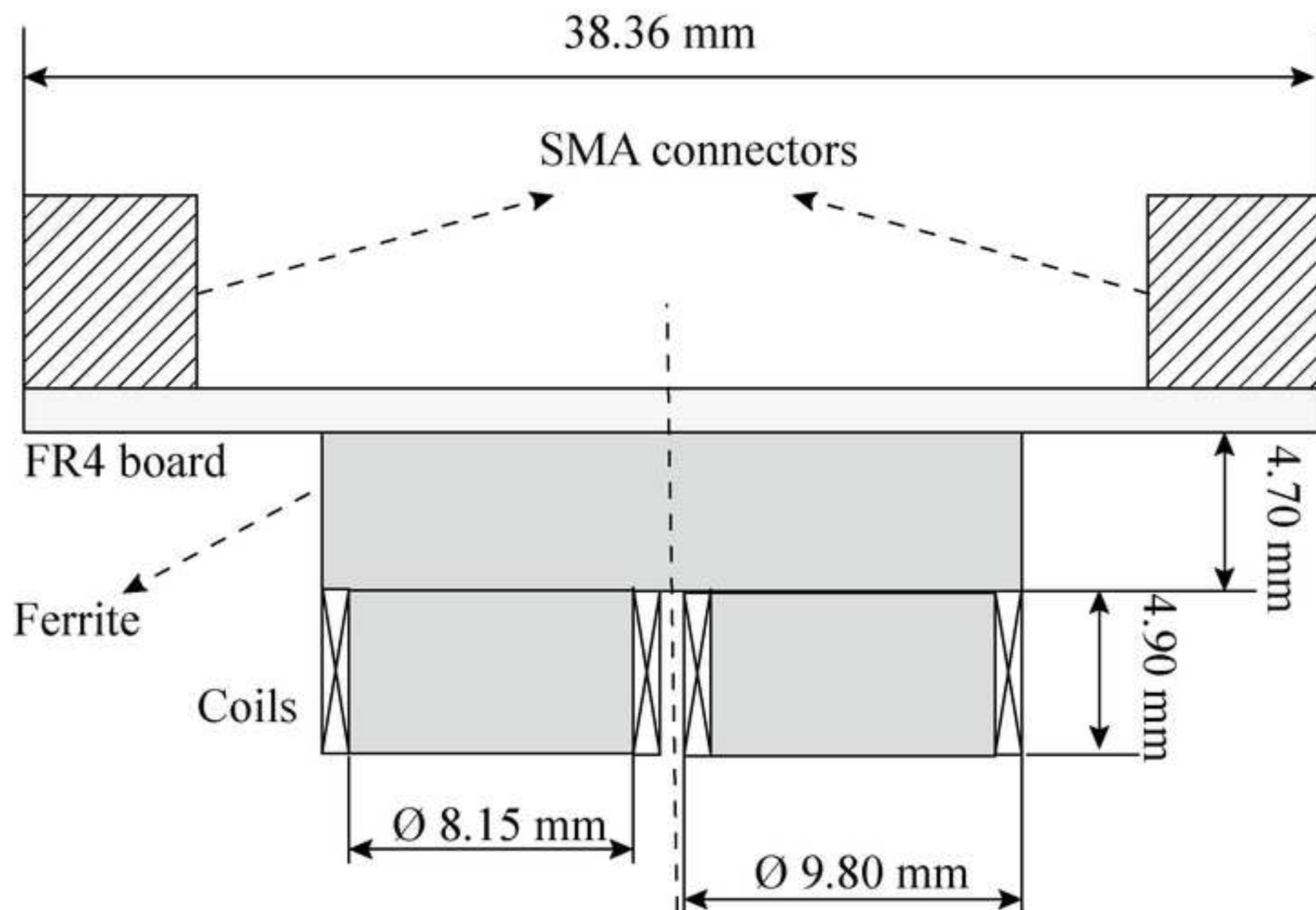




fig15.tif

[Click here to download high resolution image](#)

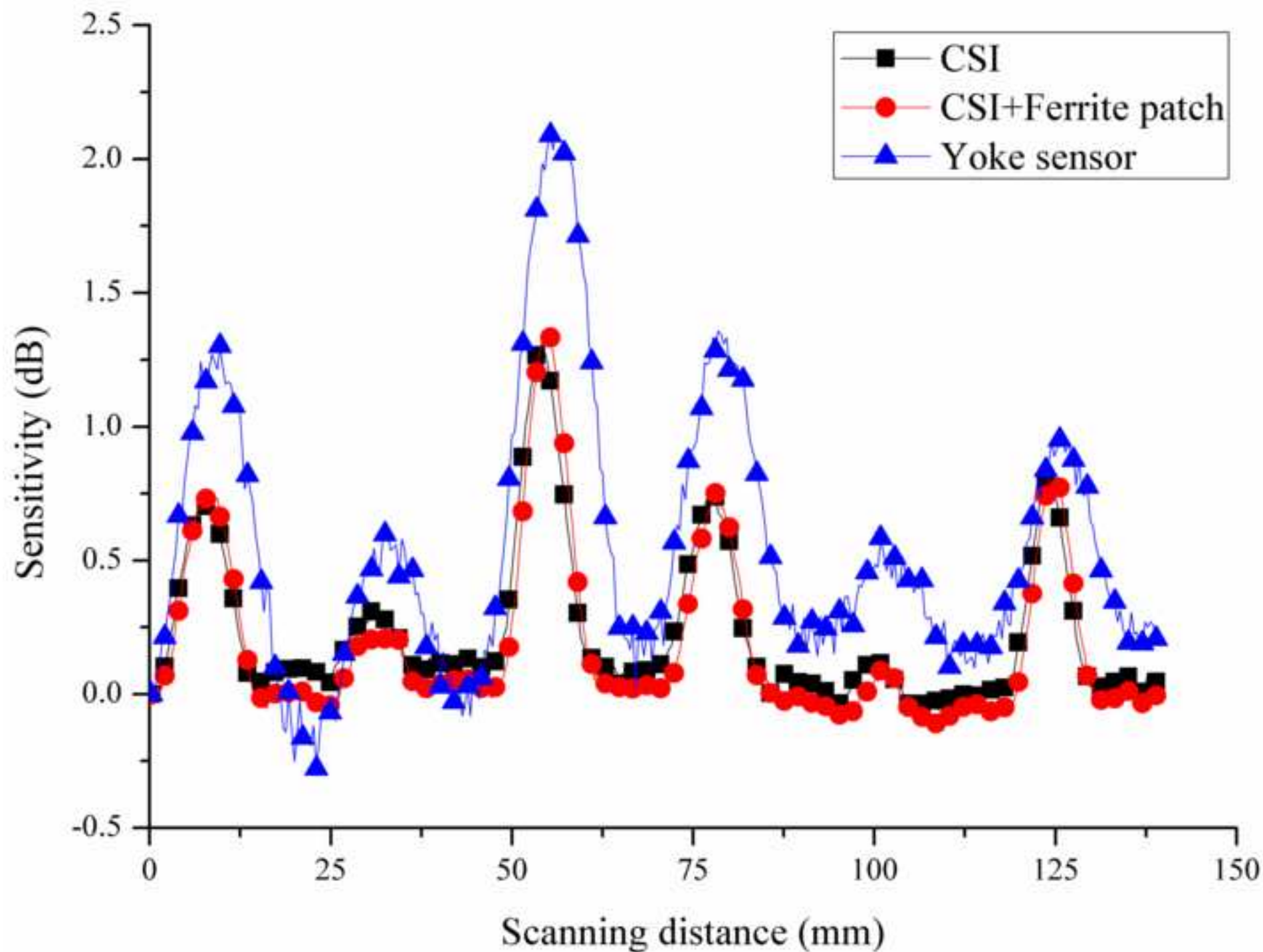
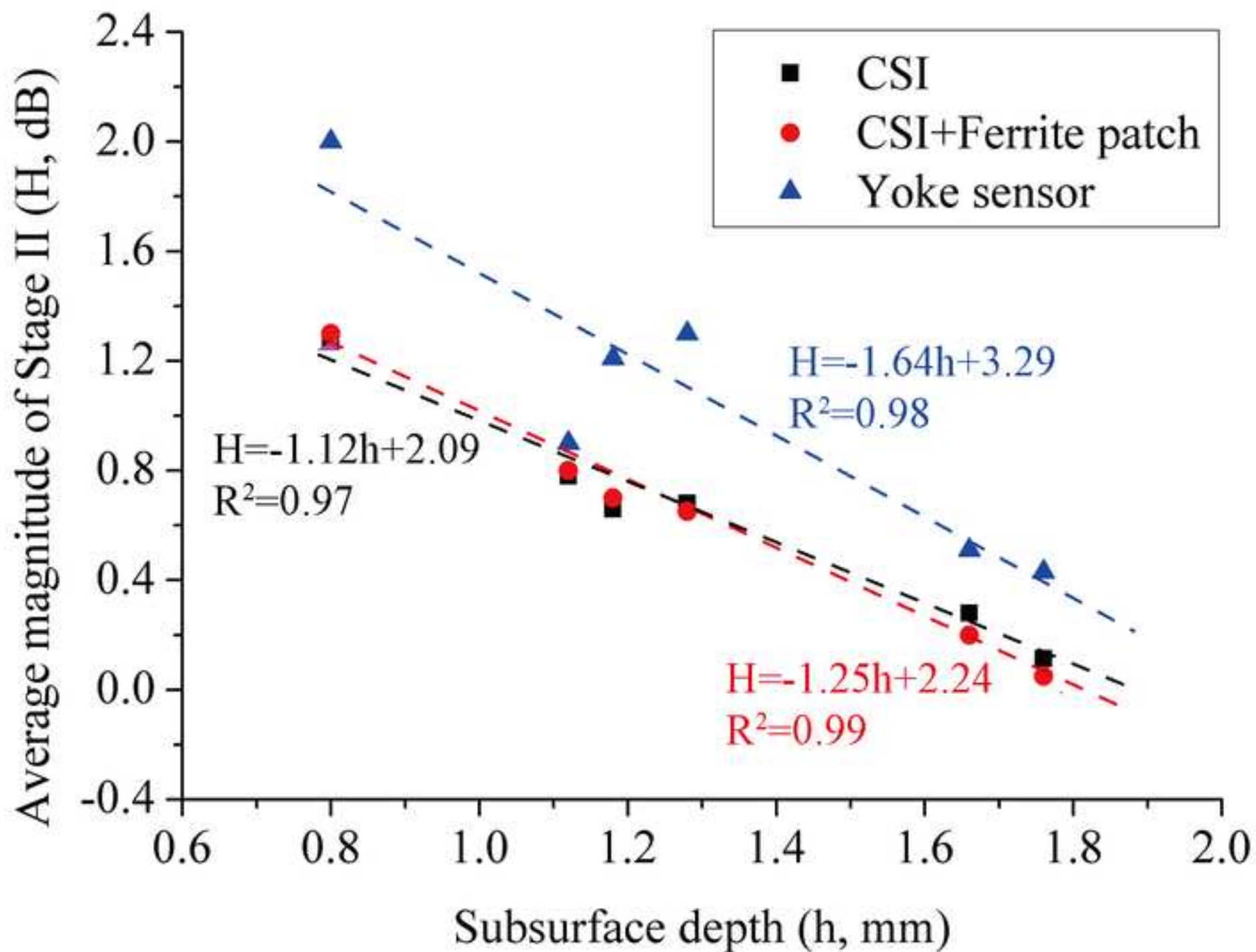
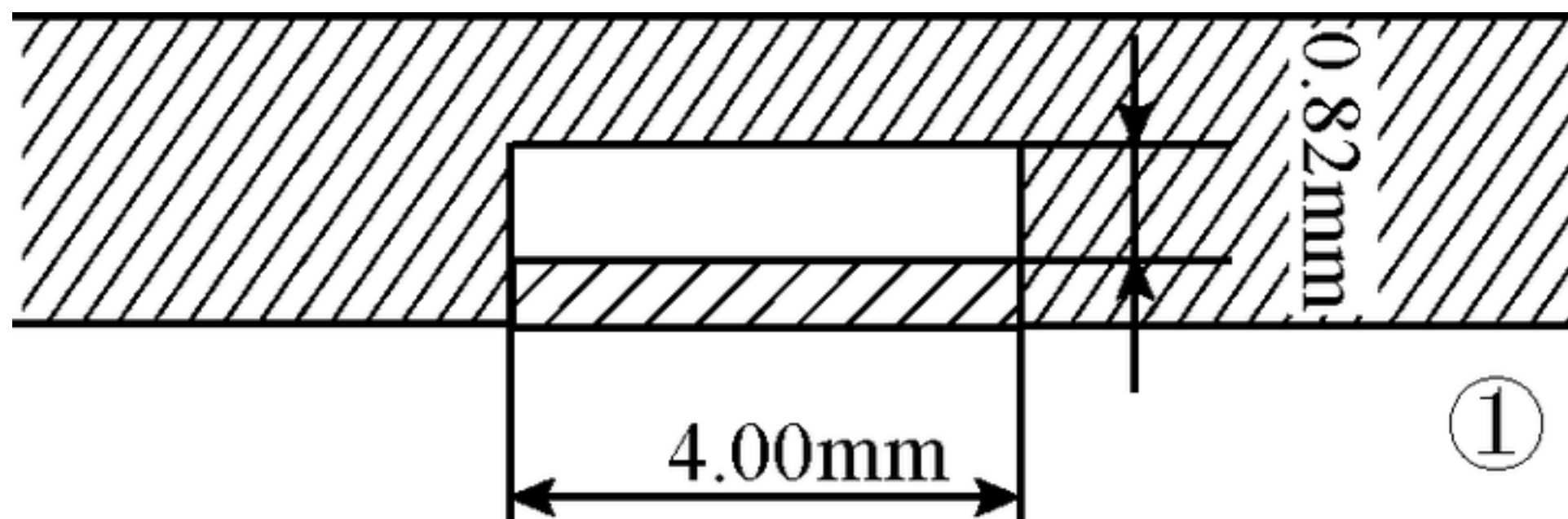
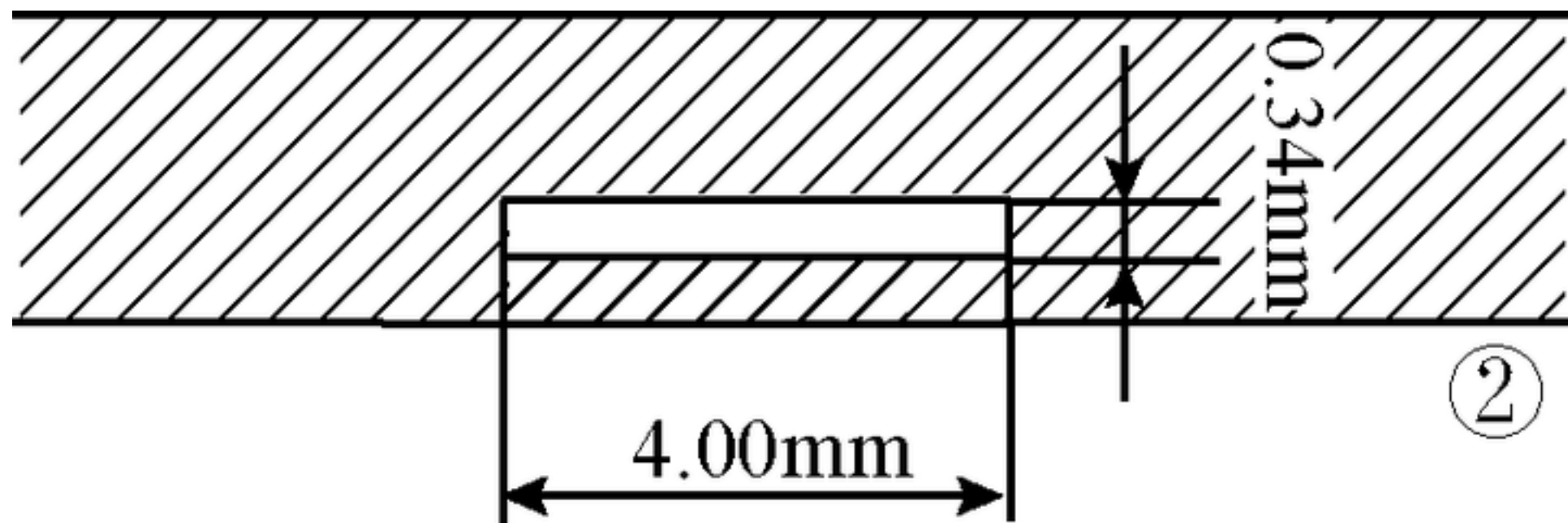


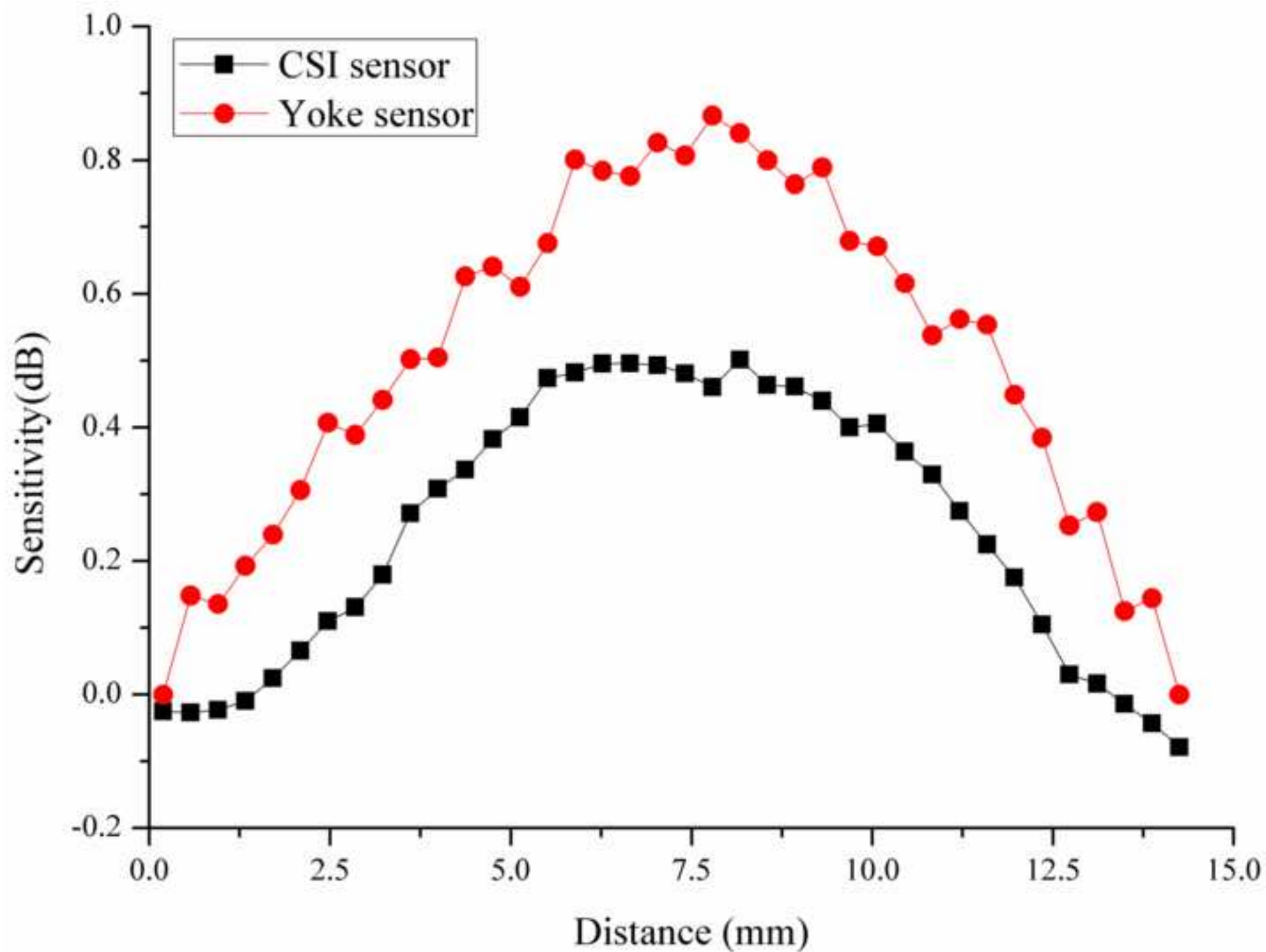
fig16.tif

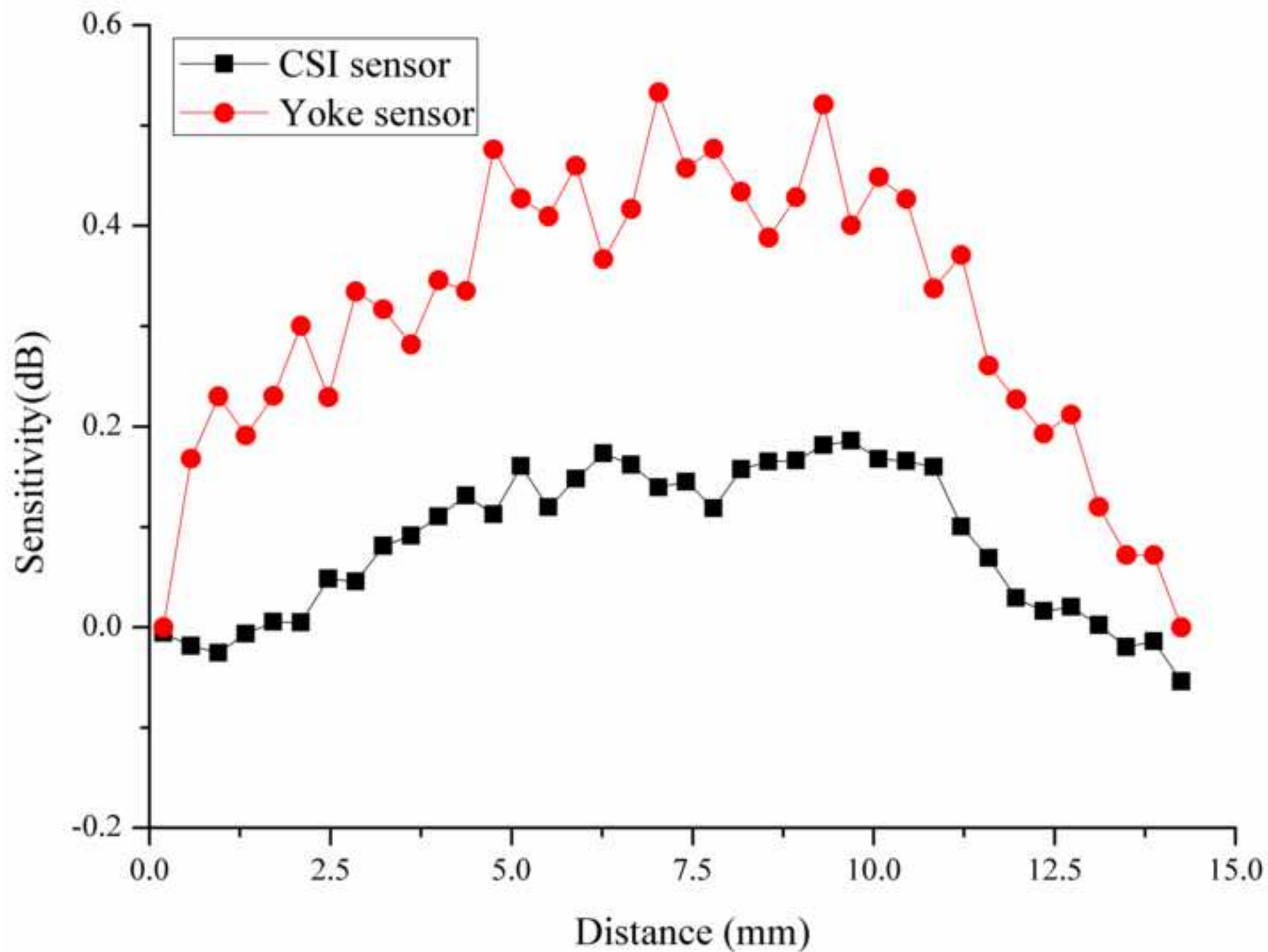
[Click here to download high resolution image](#)

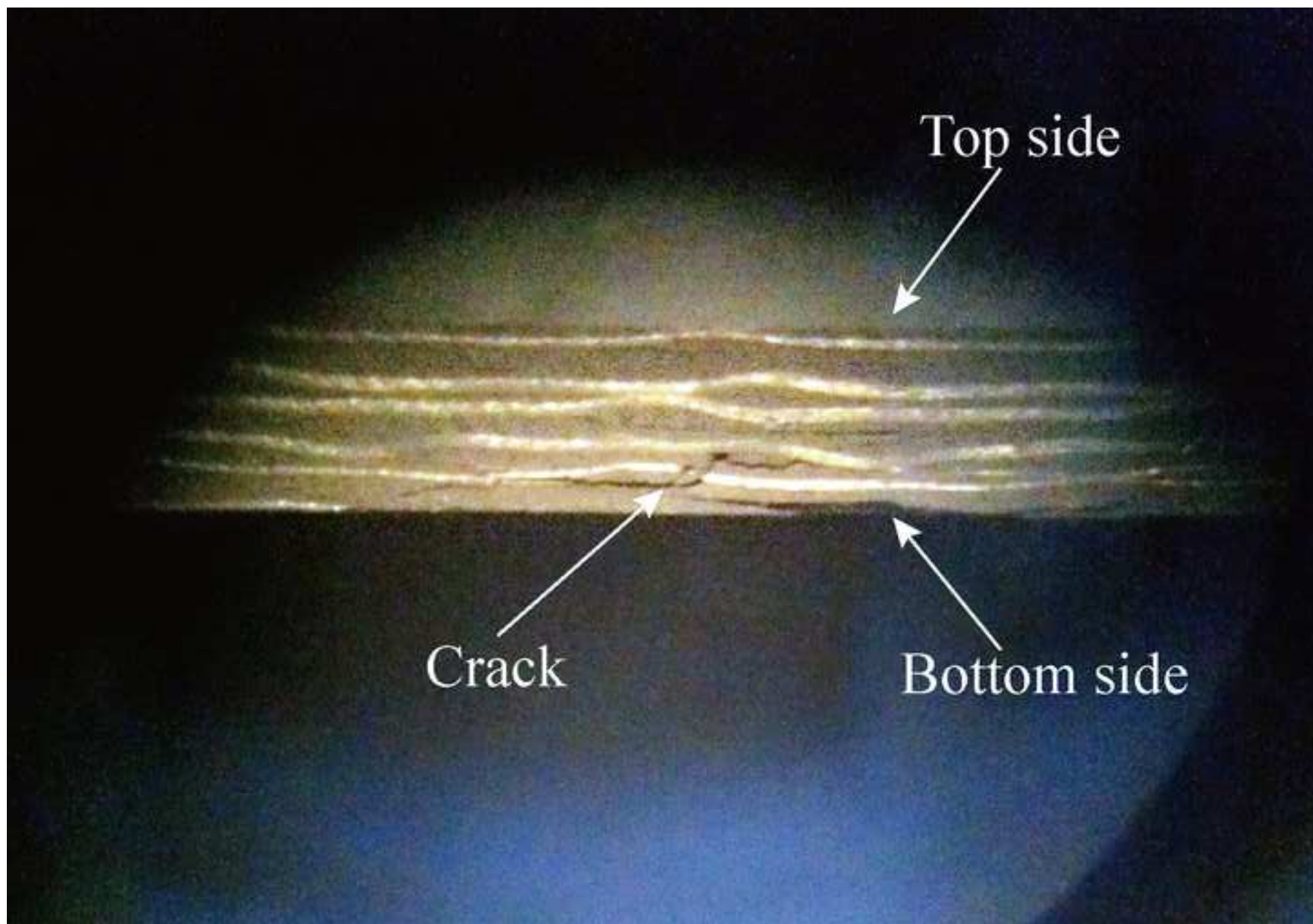


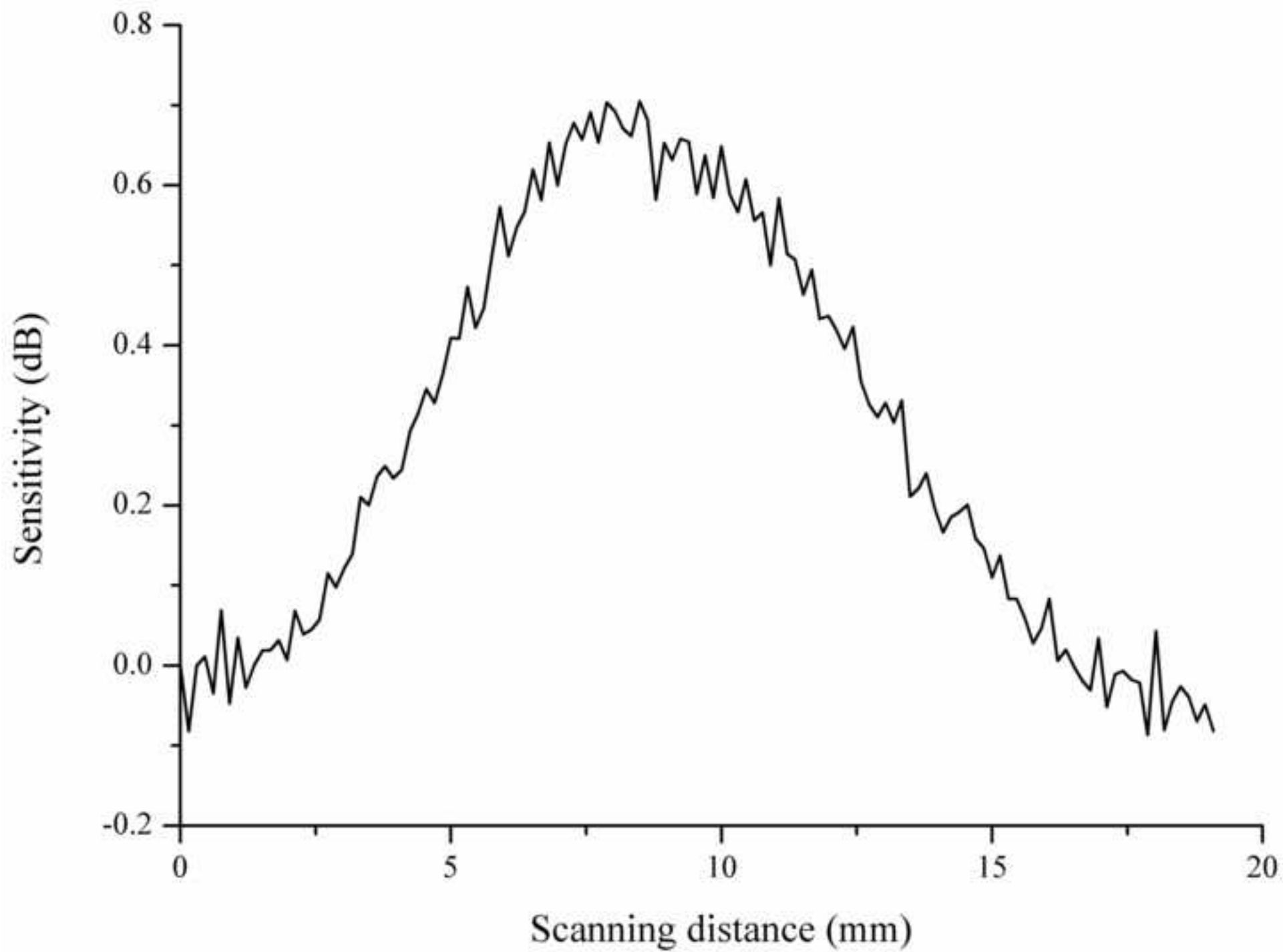












Table

Table 1 Summary of the subsurface depths of the grooves and  
the average magnitude of Stage II in the sensitivity curve

No. Groove	1 <sup>st</sup>	2 <sup>nd</sup>	3 <sup>rd</sup>	4 <sup>th</sup>	5 <sup>th</sup>	6 <sup>th</sup>
Subsurface depth (h, mm)	1.18	1.66	0.80	1.28	1.76	1.12
Average magnitude of Stage II (H, dB)	0.66	0.28	1.27	0.68	0.11	0.78